
GAZİ ÜNİVERSİTESİ
Gazi
1926

RADAR CROSS SECTION ANALYSIS OF AN AESA RADAR ANTENNA MODEL

Ömer Burak GÜNGÖRDÜ

IN PARTIAL FULFILLMENT OF THE REQUIREMENTS
FOR THE DEGREE OF MASTER OF SCIENCE
IN ELECTRICAL ELECTRONIC ENGINEERING DEPARTMENT

GAZİ UNIVERSITY
GRADUATE SCHOOL OF NATURAL AND APPLIED SCIENCES

JULY 2024

ETHICAL STATEMENT

I hereby declare that in this thesis study I prepared in accordance with thesis writing rules of Gazi University Graduate School of Natural and Applied Sciences;

- All data, information and documents presented in this thesis have been obtained within the scope of academic rules and ethical conduct,
- All information, documents, assessments and results have been presented in accordance with scientific ethical conduct and moral rules,
- All material used in this thesis that are not original to this work have been fully cited and referenced,
- No change has been made in the data used,
- The work presented in this thesis is original,

or else, I admit all loss of rights to be incurred against me.

Ömer Burak GÜNGÖRDÜ

25/07/2024

RADAR CROSS SECTION ANALYSIS OF AN AESA RADAR ANTENNA MODEL

(M.Sc.Thesis)

Ömer Burak GÜNGÖRDÜ

GAZİ UNIVERSITY

GRADUATE SCHOOL OF NATURAL AND APPLIED SCIENCES

July 2024

ABSTRACT

Modern fighter platforms today come equipped with active electronically scanned array (AESA) radars. Radar cross section (RCS) is one of the key factors in aircraft survivability. Scattering from AESA antennas can be significant; therefore, understanding the RCS characteristics and implementing measures to reduce the RCS of these types of antennas is critical. In this thesis, an AESA type array antenna model was designed to fit the dimensions suitable for a fighter aircraft. The design utilizes stacked patch antenna elements, featuring high gain, low sidelobe levels, narrow beamwidth, and beam steering capability up to 60 degrees. Additionally, a radome and an underside feed network were also designed. The antenna design and analyses were conducted using the CST Microwave Studio® (CST MWS) full-wave simulator tool. Simulation results were compared with radiation patterns obtained through the pattern multiplication method. Subsequently, simulations and computations were performed to analyze the antenna mode and structural mode scattering of the designed antenna. The results demonstrated that scattering from AESAs can be substantial, and reduction methods are proposed.

Science Code : 93415
Key Words: : Active electronically scanned array, AESA, radar, RCS, radar cross
Page Number : 67
Supervisor : Prof. Dr. Ali KARA

AESA RADAR ANTEN MODELİNİN RADAR KESİT ALANI ANALİZİ

(Yüksek Lisans Tezi)

Ömer Burak GÜNGÖRDÜ

GAZİ ÜNİVERSİTESİ

FEN BİLİMLERİ ENSTİTÜSÜ

Temmuz 2024

ÖZET

Günümüz modern savaş uçağı platformları, aktif elektronik taramalı dizi (AESA) radarları ile donatılmıştır. Radar kesit alanı (RKA), uçakların hayatta kalabilirliği açısından önemli faktörlerden biridir. AESA antenlerinden kaynaklanan saçılma önemli olabilir; bu nedenle, bu tür antenlerin RKA özelliklerini anlamak ve RKA'sını azaltmak için önlemler almak kritik önem taşır. Bu tezde, bir savaş uçağına uygun boyutlarda bir AESA tipi dizi anten modeli tasarlanmıştır. Tasarım, yüksek kazanç, düşük yan lob seviyeleri, dar huzme genişliği ve 60 dereceye kadar huzme yönlendirme yeteneği sunan katmanlı yama anten elemanları kullanmaktadır. Ayrıca, bir radom ve alt besleme ağı da tasarlanmıştır. Anten tasarımı ve analizleri, CST Microwave Studio® (CST MWS) tam dalga simülatör aracı kullanılarak gerçekleştirilmiştir. Simülasyon sonuçları, ışıma örüntüsü çarpma yöntemi ile elde edilen radyasyon örüntüsü ile karşılaştırılmıştır. Daha sonra, tasarlanan antenin anten modu ve yapısal mod saçılımını analiz etmek için simülasyonlar ve hesaplamalar yapılmıştır. Sonuçlar, AESA'lardan kaynaklanan saçılmanın önemli olabileceğini göstermiş ve azaltma yöntemleri önerilmiştir.

Bilim Kodu : 93415
Anahtar Kelimeler : Aktif elektronik taramalı faz dizinli anten, AESA, radar, RKA,
Sayfa Adedi : 67
Danışman : Prof. Dr. Ali KARA

ACKNOWLEDGEMENTS

I would like to express my deepest gratitude to my advisor, Prof. Dr. Ali KARA, for his invaluable guidance, encouragement, and unwavering support throughout my thesis study. His profound knowledge and insightful feedback have been instrumental in shaping this work.

I extend my heartfelt thanks to my family and friends for their continuous encouragement, patience, and understanding. Their support has been a constant source of strength and motivation throughout this journey.

I am also profoundly grateful to Turkish Aerospace for their generosity in providing me with the necessary resources and cooperation. Their commitment to fostering an environment conducive to research has been invaluable. Additionally, I would like to thank my dear colleagues for their unwavering support, insightful discussions, and camaraderie, which have greatly contributed to the successful completion of my studies.

CONTENTS

Page

ABSTRACT iv

ÖZET v

ACKNOWLEDGEMENTS vi

CONTENTS vii

LIST OF TABLES ix

LIST OF FIGURES x

SYMBOLS AND ABBREVIATIONS xii

1. INTRODUCTION 1

2. BACKGROUND INFORMATION 5

2.1. Radar 5

2.2. Active Electronically Scanned Array Radar 7

2.3. Radar Cross Section 9

2.4. Radar Cross Section of Antennas 11

2.5. Radar Cross Section Reduction 12

3. ANTENNA DESIGN 13

3.1. Antenna Element Design 13

3.2. Unit Cell Design 23

3.3. Phased Array Theory, Design and Analysis 27

3.3.1. Array architecture 28

3.3.2. Phase scanning for planar arrays 30

3.3.3. Element pattern 32

3.3.4. Taylor pattern synthesis 34

3.3.5. Array design and analysis 35

4. ANTENNA RCS THEORY AND RESULTS 49

4.1. Antenna RCS Computed from Gain 49

Page

4.2. Antenna Scattered Field as a Function of Load Impedance……..... 50

4.3. Antenna RCS Results……... 51

5. CONCLUSION…… 61

REFERENCES..... 63

RESUME 67

LIST OF TABLES

Table **Page**

Table 3.1. Effect of dimensions on the antenna element performance 16

Table 3.2. Antenna element parameter values 16

Table 3.3. Microstrip transmission line parameters. 24

Table 3.4. Values of constant B for specified SLL 35

Table 3.5. Summary of array radiation pattern (uniform illumination) 38

Table 3.6. Array radiation patterns summary with different scan angles 44

LIST OF FIGURES

Figure **Page**

Figure 2.1. Monopulse antenna patterns 6

Figure 2.2. MSA vs AESA beam steering performance 8

Figure 2.3. Monostatic and bistatic RCS configurations 11

Figure 2.4. RCS representation of an array antenna element 11

Figure 3.1. Electrical model of stacked patch antenna 14

Figure 3.2. Cross section side view 15

Figure 3.3. Cross section top view (dielectric not visible) 15

Figure 3.4. Patch antenna 3D model 17

Figure 3.5. Return loss $S11$ Plot 18

Figure 3.6. Maximum Gain vs Frequency 19

Figure 3.7. f=9 GHz radiation pattern polar plot 20

Figure 3.8. f=9.5 GHz radiation pattern polar plot 20

Figure 3.9. f=10 GHz radiation pattern polar plot 21

Figure 3.10. f=10.5 GHz radiation pattern polar plot 21

Figure 3.11. Cross-polarization pattern at f=10 GHz 22

Figure 3.12. 3D radiation pattern at f=10 GHz 22

Figure 3.13. Quarter wave transformer 23

Figure 3.14. Microstrip on a substrate 24

Figure 3.15. Unit cell 3D Model 25

Figure 3.16. Unit cell S11 dB 26

Figure 3.17. Maximum gain over frequency 27

Figure 3.18. f=10 GHz radiation pattern polar plot 27

Figure 3.19. Basic array construction types 29

Figure **Page**

Figure 3.20. Combining of subarray channels 30

Figure 3.21. Planar array geometry..... 30

Figure 3.22. Full array model consisting of 75 AESA modules with containing 16 antenna elements 36

Figure 3.23. Full array radiation pattern at with different frequencies 38

Figure 3.24. Active element return loss. 39

Figure 3.25. Radiation pattern at f=10 GHz 40

Figure 3.26. Radiation pattern with different frequencies 41

Figure 3.27. CST and synthesized radiation pattern comparison 42

Figure 3.28. Radiation pattern array scanning 43

Figure 3.29. 3D radiation pattern for 60-degree elevation scan angle..... 44

Figure 3.30. Insertion loss $S21$ plot..... 47

Figure 3.31. Effect on full array radiation performance 47

Figure 4.1. Matched load RCS pattern with different polarized incident waves at f=10 GHz 53

Figure 4.2. Matched load RCS pattern with radome and different polarized planes waves at f=10 GHz..... 54

Figure 4.3. Scattering 3D pattern under y-polarized incident wave 55

Figure 4.4. Matched load RCS versus frequency with and without radome. 55

Figure 4.5. Effect of tilting the array on structural mode scattering..... 56

Figure 4.6. ML-RCS when plane wave incident on ϕ=90°, θ=-20° at 10GHz (xz plane)..... 57

Figure 4.7. Antenna mode RCS with radome and feed network included 58

Figure 4.8. Antenna mode RCS with different configurations 59

SYMBOLS AND ABBREVIATIONS

The symbols and abbreviations used in this study are presented below, along with their explanations.

Symbols	Explanations
3D	Three Dimensions
GHz	Gigahertz
J0	Bessel Function
Ω	Ohm
dB	Decibel
dBi	Decibel Isotropic
dBsm	Decibel Square Meter
f0	Center Frequency
ϵ	Epsilon
τ	Pulse Width
Γ	Reflection Coefficient
σ	Radar Cross Section
P_t	Peak Transmitter Power
A_e	Antenna Aperture Size
Δt	Delta Time
Q	Quality Factor
λ_g	Guided Wavelength
dBm	Decibel Milliwatts
λ	Wavelength

Abbreviations	Explanations
AESA	Active Electronically Scanned Array
AMC	Artificial Magnetic Conductor
BW	Bandwidth
CPCM	Checkerboard Polarization Conversion Metasurface
CW	Continuous Wave

Abbreviations	Explanations
EM	Electromagnetic
FEM	Finite Element Method
FSS	Frequency Selective Surface
HVPS	High Voltage Power Supply
LNA	Low Noise Amplifier
LPI	Low Probability of Intercept
MMIC	Monolithic Microwave Integrated Circuits
MSA	Mechanically Scanned Array
PBA	Perfect Boundary Approximation
PCB	Printed Circuit Board
PW	Pulse Width
RADAR	Radio Detection and Ranging
RCS	Radar Cross Section
RCSR	Radar Cross Section Reduction
RF	Radio Frequency
SF	Space Factor
SLL	Side Lobe Level
SNR	Signal to Noise Ratio
SSPA	Solid State Power Amplifier
T/R	Transmit/Receive
TWT	Travelling Wave Tube
VGA	Variable Gain Amplifier

1. INTRODUCTION

AESA Radar is a type of multifunctional radar that contains transmit-receive (T/R) channel for each individual radiating element. AESA antenna is a type of antenna can steer and shape beams electronically by controlling the phase and amplitude on each T/R channel. AESA radars offer several key advantages, making them very popular among modern fighter platforms. These include high bandwidth, advanced mode interleaving for radar multifunctionality, and support for multiple weapons launching. They are also known for their reliability, low observability, and extreme beam agility, which enhance targeting precision and stealth [1]. These features collectively ensure superior performance in combat scenarios. A typical fighter AESA antenna unit is composed of several key components: T/R modules, radiating elements, RF manifolds, a radome, a power supply, a cooling interface, and a control card for interfacing with other systems [2]. An array antenna can be a significant scattering source for fighter platforms, potentially disrupting their stealth characteristics and reducing their survivability. Therefore, mitigating and understanding the radar cross section (RCS) of AESA antennas is quite significant when designing a stealth platform. In this article an array antenna that has a geometry and features that is suitable for a fighter platform has been designed; along with an inner radome and an underside feed network for a single tile module to conduct RCS analysis.

Antenna scattering is different from generic object scattering due to its two modes of scatter rather than one. The first mode, known as structural mode scattering, is determined by the antenna's shape, material, and size. This type of scattering is independent of whether the scatterer is an antenna or not [3]. Various methods exist to mitigate the structural mode RCS of an antenna. One highly investigated method involves integrating a metasurface with the antenna. Metasurfaces are appealing because they can alter the polarization and phase of incident electromagnetic waves, enabling scattered field cancellation and effectively reducing the antenna's RCS. However, this approach introduces additional structures to the array and comes with performance trade-offs [4]. Another effective method to reduce antenna RCS involves using Frequency Selective Surface (FSS) based aircraft radomes, which are commonly used in modern fighter jets to enhance stealth capabilities [5, 6].

The second mode of scattering is called antenna mode scattering, which depends solely on

the antenna's radiation characteristics. The relationship between gain and antenna mode backscattering has been well established. Numerous studies have examined antenna mode scattering. For instance, Appel-Hansen [7] derived the relationship between an antenna's radiation properties and its scattering, excluding the structural mode scattering. This derivation has been utilized to analyze antenna mode RCS in this paper. Several references investigate patch antenna backscattering under different loading conditions (short-circuited, match-loaded, and open-circuited), concluding that antennas with various arbitrary loads exhibit similar RCS characteristics, and highest scattering occurs when antenna is terminated with a short circuit load [8-11].

Array antennas have the same scattering components as other antennas but also has additional complications due to their can be complex feed networks and mutual coupling effects within the array [3]. These complications make estimating the antenna mode RCS of arrays challenging. There are multiple published works that provide an analytical estimation of antenna mode RCS. For example, authors at [12] predict RCS for large airborne array antennas using a modified expression derived from Appel-Hansen's paper. However, this estimation overlooks the effect of the feed network and mutual coupling effects in array antennas and it is based on simple array theory. Another related study, conducted in [13], predicts the antenna mode RCS using a method called the active element scattering pattern, which is based on the active element pattern method. Inner smaller arrays, known as sub-array, scattering patterns within a full array environment are analyzed then multiplied as inner elements exhibit similar scattering characteristics. This method significantly reduces simulation time and takes mutual coupling and edge effects into consideration.

One of the key advantages of AESAs over mechanically steered arrays (MSAs) is facilitating a lower RCS of the platform. MSAs can have a higher RCS relative to the receiver than AESAs due to the antenna being positioned towards the locked target whilst tracking when in single tracking mode, whereas in AESAs the antenna has a fixed position on the platform. Additionally, the moving parts of the MSA radars also contribute to the structural mode RCS of the platform [14]. Furthermore, AESAs have shorter RF path lengths compared to MSAs, which have more complex feed designs, resulting in lower losses at the front end [1]. Therefore, antenna re-radiations are minimized on AESAs. Another aspect affecting RCS is aperture size. Due to their fixed positions, AESAs

comparatively have larger apertures [15], resulting in an increase in both scattering modes.

In this paper, a microstrip patch antenna array has been selected as the target due to its preference for AESA radar systems for the ones installed on older fighter platforms. Microstrip patch antennas are favored for their compact size, low cost, and ease of integration into the rest of the system [16]. Despite their lower bandwidth compared to notch elements, they offer a more practical solution. Designing a broadband patch antenna that maintains a compact size and high gain presents significant challenges, thus a compact sized stacked patch antenna with relatively high bandwidth and gain is designed and presented.

Additionally, while some AESA radar functions may require dual polarization, this adds complexity and necessitates trade-offs [17]. Therefore, for only RCS analysis purposes, a single-polarized antenna design solution has been proposed. Using this patch antenna model, an array consisting of 1200 elements has been designed.

To analyze the RCS of the antenna more accurately, an underside feed network has been designed for 16 antenna elements to replicate the losses caused by the T/R module circuit board. Additionally, AESA antennas with tile construction are usually integrated with a radome to protect the antenna from external conditions. To simulate any losses caused by the radome, a monolithic radome has been designed. To estimate the structural mode returns, a full-wave simulator has been utilized when the array antenna ports are terminated with a matched load. To compute the antenna mode scattering, the relationship between the gain of the antenna and antenna mode scattering has been used. Antenna mode RCS with different configurations has been analyzed.

The thesis is structured as follows: Chapter 2 provides background information on topics such as radars, AESAs, RCS, and RCS reduction techniques. Chapter 3 presents the antenna array design description, analysis results, and background theory. Chapter 4 covers the theory of antenna RCS computation and presents the RCS analysis results of the proposed antenna. Chapter 5 summarizes the thesis results and contributions. Chapter 6 includes future work and a discussion.

2. BACKGROUND INFORMATION

2.1. Radar

The acronym radar stands for "radio detection and ranging", and it has been developed in the late 1940s to replace visual target detection. Radar is a system used to detect and locate objects by transmitting some sort of electromagnetic (EM) waveform and detect the correspondent echo signal. Radar system uses the known velocity of an EM wave to determine the distance from a target, which is $c = 3 \times 10^8$ meters per second. The range to the target is calculated by measuring the time Δt it takes pulse to arrive to the target and return. The range to the target is given by [18];

$$R = c\Delta t \, / \, 2 \tag{2.1}$$

Knowing the range alone is not enough to determine the location of the target. Two-way direction angles to the target must be calculated. For mechanically scanned radars, the target angle can be measured by simply calculating the azimuth and elevation angles the antenna is pointed towards [3]. Angles in both directions can be determined by gimbal system. The range and the angles on azimuth and elevation can be used to determine the location of the target and its future positions along with doppler shift. For tracking radars method used for angle measurement is what separates it from other radars [18]. For systems that utilize electronically scanned arrays monopulse angle measurement technique is the most common angle tracking method [19]. In this technique the multiple closely spaced beams are formed and received from the same antenna. A sum beam pattern is used for transmission and both the sum and difference patterns are used on receive mode. The difference pattern is used in receive mode gives the magnitude of the error angle. The sum pattern is used for range measurements and reference for angle measurement. All the information necessary to determine the target position can be obtained with a single pulse therefore this technique is called monopulse. The receive angle can also be determined by comparing the phases between separate antennas; this technique is called phase-comparison monopulse. This technique is less popular for tracking radars due to higher sidelobes on receive pattern caused by large distance between the subarrays [1], [18].

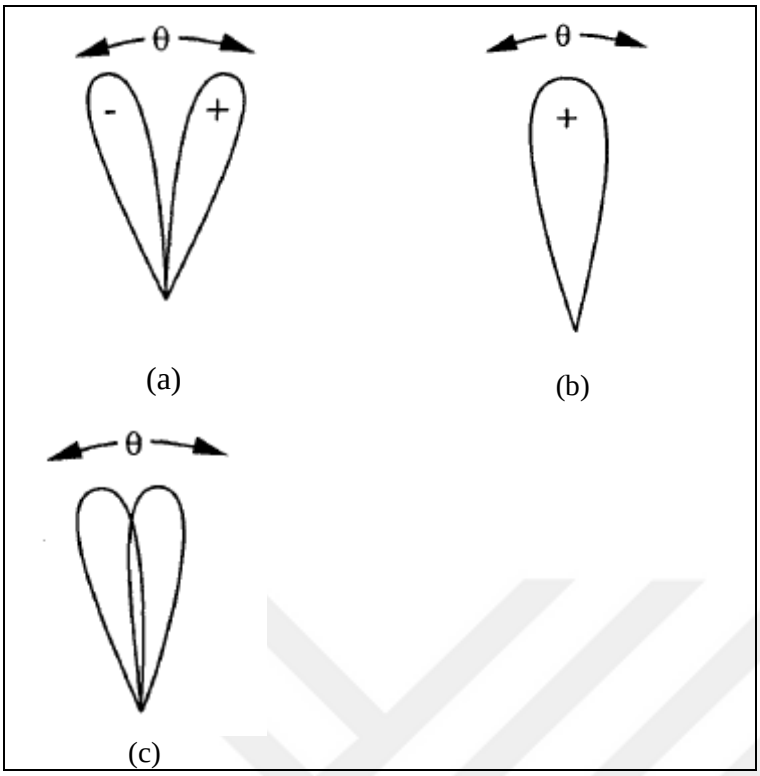


Figure 2.1. Monopulse antenna patterns (a) difference pattern (b) summation pattern (c) squinted antenna pattern [18]

Pulsed radars and continuous wave are the two main types of radars. Pulse radars transmit high power burst of energy and then listen to echoes for the duration between pulses. This allows for precise range measurement by calculating the time delay between transmission and reception. Continuous wave (CW) radars on the other hand emit a constant waveform and leverage the doppler frequency shift to separate the echo from the transmitted signal. Frequency or phase modulations is necessary for range measurements as unmodulated CW signals can't be used to measure range. Fire control radars use pulsed radar types as they can emit high powered short pulses to resolve target at higher ranges. Ratio of pulse width (τ) and pulse repetition period is called the duty cycle. Airborne pulsed radars have a typical duty cycle value of 1% to 20% for air-to-air tracking modes while continuous wave radars have infinite duty cycle [1], [18].

The radar range equation is a great way to understand radar operation and effect of target radar cross section on radar range. The fundamental radar range equation given as [18]

$$R_{max} = \left[\frac{P_t G A_e \sigma}{(4\pi)^2 S_{min}}\right]^{1/4} \tag{2.2}$$

Where P_t is the peak transmitter power, G is the gain of the radar antenna, σ is the radar cross section of the target, A_e is the receiving antenna aperture size, S_{min} is minimum detectable signal and R_{max} is the maximum radar range which targets beyond this range are undetectable [18]. Radar range equations although useful for understanding what effects radar range, it does not fully represent radar performance due to many assumptions being made. Fully understanding radar range equation is necessary for RCS reduction tasks. As it can be used to investigate the effect of RCS on radar range performance. Although the equation assumes target has a non-fluctuating RCS characteristic [3].

2.2. Active Electronically Scanned Array Radar

Nowadays, the majority of advanced fighter aircraft are equipped with Active Electronically Scanned Array radars. It is a type of multifunctional radar that each radiator has its own transmit-receive channel. Modern fighter platforms favor AESA radars because of their high bandwidth, advanced mode interleaving capabilities, support for launching multiple weapons, reliability, low observability, power efficiency and digital beamforming abilities [1]. One of the key technologies that enables AESA radar is the microwave integrated circuits (MMIC). These circuits enable low cost, reliable, power efficient, smaller volume systems [15]. GaN based solid-state power amplifier (SSPA) integrated T/R modules has the capability to have high peak power up to 20 watts per element with high instantaneous bandwidth [20].

The most important element of an AESA is the T/R modules. There are many design considerations such as types of circuit element required, power output, RF coupling between elements, transmission loss, precise amplitude and phase control etc. The basic module compromises circuit elements such as SSPA (typically GaN or GaAs based), low noise amplifier (LNA), driver amplifier, phase shifter, circulator, variable-gain amplifier (VGA), digital control circuit etc. Modern SSPAs for AESA applications are usually have been made of GaN. It has superior thermal conductivity and power efficiency compared to GaAs SSPAs [15].

Some of the must have parameters of AESA Radars are high volume density to support half wavelength spacing between the antenna elements to have optimal scanning performance, high computing power to calculate beam mapping and adjustments in msecs,

auto gain control, high power densities and efficiency, low coupling between T/R modules, phase and amplitude control to support multiple receive and transmit patterns. High speed data transfer is needed for fast beam controls so typically a gigabit ethernet interface is used between the antenna and the radar computer [1].

One of the most important advantages of AESA Radar compared to older mechanically steered array (MSA) is the extreme beam agility. MSA Radar beam steering capability is limited to its gimbal mechanism, which can scan between 100 and 150 degrees per second. On the contrary, AESAs can scan a ±60-degree cone less than an msec [15]. This capability enables AESAs to track multiple targets with single-target tracking level accuracy and perform multiple radar functions (or modes) by time interleaving their data. Each mode has its own respective module responsible for its function [1].

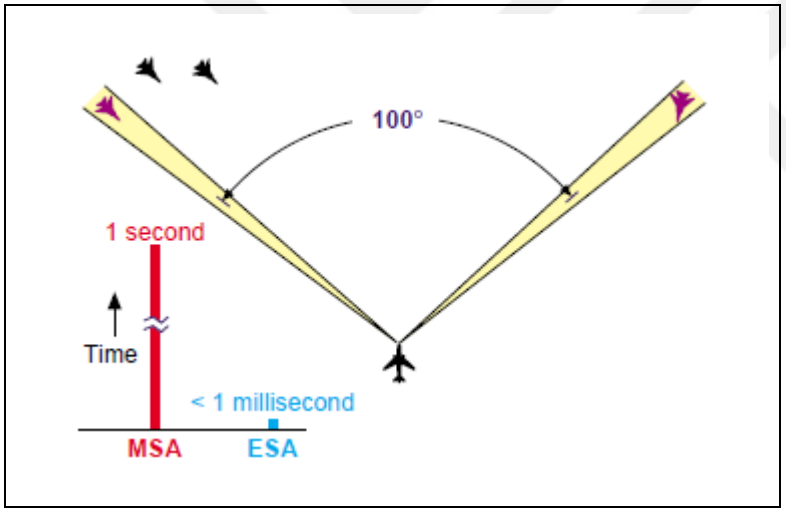


Figure 2.2. MSA vs AESA beam steering performance [15]

AESA Radars are much more reliable than MSAs due to elimination of gimbal system and moving parts. All of these parts are highly fail prone. Additionally, AESAs replaces the central travelling wave tube (TWT) power amplifier with T/R module's SSPAs. The TWTs and their high-voltage power supply (HVPS) are reportedly very unreliable and difficult to maintain. And with potential failure whole system becomes nonoperational as opposed to AESAs where system can still be operational even if some of the T/R modules fail. There would be no serious degradation to performance even with 5% of the modules fail [1].

AESA radars have a typical duty cycle value of 10% to 20% for air-to-air tracking modes.

Power amplifiers for transmitting in AESA radars are capable of generating high average power but can generate low total peak power compared to TWTs found on older generation airborne radars [1]. That is why it is required to have high duty cycle for efficient energy transmission. This disadvantage in lower peak power can be compensated by using more pulse compression and by having wider bandwidth [15].

Another important metric of radar antennas is the RCS characteristics as scattering from an even small planar antenna can be substantial [3]. So, RCS reduction methods must be used to not disrupt the stealth characteristics of the aircraft. MSA fire control radars found on older fighter platforms can have higher RCS in the incident wave direction than AESA Radar antennas because the antenna is always positioned towards the locked target with a gimbal whereas in most AESA Radars antenna is positioned still. Therefore, RCS of AESAs can be reduced in incident wave direction by tilting the antenna upwards to avoid mirror like reflections. This method obviously not applicable for MSAs due to no electronic scan capability [15]. Other RCS reduction methods are mentioned in Section 2.5.

Moving parts of the mechanically steered radars are also a contributor to the overall platform RCS [14]. AESA antennas offer advantages in terms of reduced RF path lengths, leading to lower losses at the front end [1]. This would have resulted into having better antenna mode RCS but their aperture size is usually larger than MSA due to no gimbal movement space, which effects both antenna mode and structural mode RCS. Despite this, AESA antennas are superior in terms of low probability of intercept (LPI) making them well suited for stealth platforms.

2.3. Radar Cross Section

RCS measures the scattered power when an electromagnetic wave strikes a target. It depends on factors such as the target's orientation relative to the radar transmitter and receiver, the target's shape and material, the wavelength of the incident wave, the polarization of both the transmitter and receiver, among other parameters. RCS is normalized to the power density of the incident wave at the target; therefore, it is independent of the target's distance from the illumination source. Radar cross section can be expressed as [3]

$$\sigma = \lim_{r\to\infty} 4\pi r^2 \frac{|\mathrm{E_s}|^2}{|\mathrm{E_i}|^2} \tag{2.3}$$

Where $\mathrm{E_s}$ is the scattered electric field, $\mathrm{E_i}$ is the incident electric field, R is the distance from the target. The unit for radar cross section is σ is area, usually depicted as square meters or in dB scale dBsm. This definition can be re-written in terms of radar range equation for received power by the radar as [3]

$$P_r = \frac{\left(\frac{P_t G_t}{4\pi R^2}\right)\sigma}{4\pi R^2}(A_e) \tag{2.4}$$

Where G_t is transmitter antenna gain. First term of the numerator represents the power density of the target due to transmitter.

There are three cases of scattering. Monostatic scattering case is when the receiver and the transmitter are collocated, in this configuration radar system uses the same antenna for both transmitting and receiving. In this configuration only the orientation angles of the target relative to the transmitter is needed [3].

Bistatic scattering case is when the transmitter and receiver are in different coordinates. In this configuration both the orientation angles of the target relative to the transmitter and receiver are needed [3].

Forward cross section quantifies the power scattered by an object in the same direction as the incident electromagnetic wave. Scattered power is typically 180° out of phase with the incident field, leading to destructive interference when combined with the incident wave. This phase relationship results in a shadow region behind the object, where the wave intensity is significantly reduced [3].

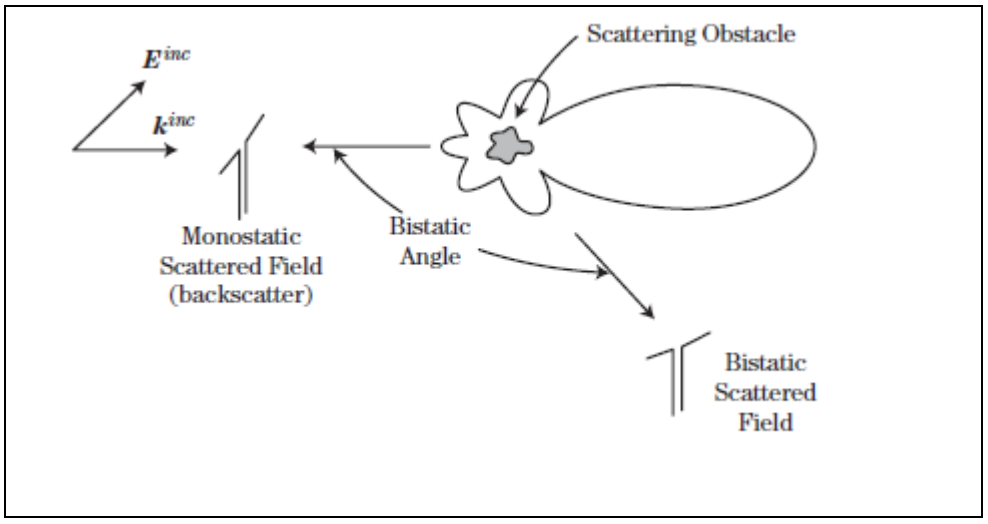


Figure 2.3. Monostatic and bistatic RCS configurations [3]

2.4. Radar Cross Section of Antennas

Objects considered as antenna has two possible modes of scattering rather than one described in Section 2.3. The first mode of scattering is called the structural mode scattering, and it occurs due to antenna's shape, size, and material. It occurs due to antenna's physical properties and it is independent from the antenna's load. It is also defined as the scattering arises from the antenna when antenna is terminated with matched load. The other mode of scattering is called the antenna mode scattering, and it occurs due to the sole fact that scattering is an antenna, i.e. a structure designed to transmit and receive RF energy. It occurs when an electromagnetic wave is incident on the antenna and re-radiations caused as wave travels down on the transmission line. Antenna mode RCS mainly depends on the antenna's radiation characteristics and reflection coefficient of the antenna [21]. Figure 2.4 shows a simplified RCS representation for both cases of scattering for arrays.

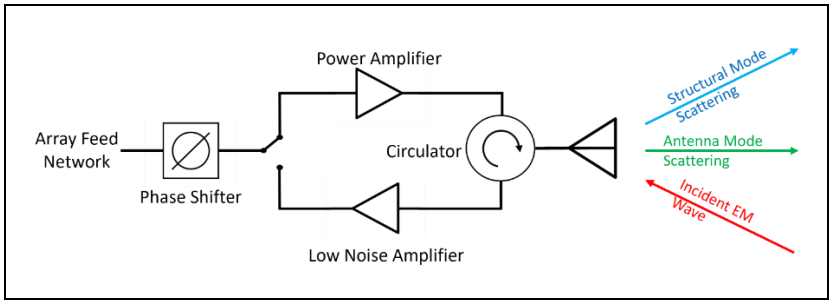


Figure 2.4. RCS representation of an array antenna element [22]

Array antennas have the same two modes of scatterer as other types of antennas. However, antenna mode RCS is the vector sum of all antenna elements. Arrays have additional complications when computing RCS as they might have complicated feed networks and various electronic devices that contribute to the re-radiation. Another feature of arrays that may be seen in the scattering pattern, although it usually is not present in AESAs are grating lobes. If the inter-element spacing of array is larger than $(\lambda / 2)$ grating lobes may be present on the visible region. But usually, arrays are designed so that inter-element spacing is lower than half a wavelength to suppress grating lobes [3].

2.5. Radar Cross Section Reduction

RCS reduction (RCSR) for antennas fall into two modes of scattering mentioned in previous chapter; reduction of antenna mode scattering and reduction of structural mode scattering. Some of the techniques for RCSR may affect both of the scattering modes.

Structural mode RCS of antennas can be reduced by employing metasurfaces such as artificial magnetic conductors (AMC) combined with perfect electric conductors (PEC) [23], frequency selective surfaces (FSS) [24], or checkerboard polarization conversion metasurfaces (CPCM) [25-28]. These techniques help to diminish the scattering from the antenna ground RCS. However, these methods typically increase the overall size of the antenna and negatively impact the antenna's radiation performance, making them less than ideal solutions.

Another approach to reducing structural mode RCS involves using the reflection cancellation method. This technique uses different antenna elements with antiphase reflections to achieve a reduction in the antenna RCS [4], [29-30]. Despite its potential, this method, along with the use of metasurfaces, often proves impractical for airborne tracking radars due to polarization requirements and performance limitations.

Given these complications, the most viable solution for effectively reducing out-of-band RCS in airborne tracking radars is the use of an FSS-based aircraft radome [5-6]. This method offers a reasonable balance between performance and practicality, addressing the challenges posed by other techniques while effectively managing the RCS.

3. ANTENNA DESIGN

3.1. Antenna Element Design

AESA Radar antennas can consist of numerous antenna elements, such as horizontal dipoles, flared-notch elements, or microstrip patches. The choice of antenna type is closely related to the specific array architecture used in the radar system [31]. In this work a stacked microstrip patch antenna has been used as the antenna element due to its compact size, relatively higher bandwidth compared to regular patch antennas and moderate gain. The antenna element has dimensions of 14.75 mm x 14.75 mm x 1.538 mm. Its compact size allows for array interelement spacing of $\lambda/2$, enabling the array to achieve forward hemisphere steering without encountering grating lobes [31].

Microstrip antennas, commonly known as patch antennas, are highly favored in the microwave frequency range due to their simplicity and compatibility with circuit board technology [16]. Stacked patches, which include one or more conducting patches parasitically coupled to a driven patch, address the narrow bandwidth limitation by adding extra resonances in the operating band. This design retains the benefits of conventional patch antennas. Similar to the basic pin-fed rectangular patch, the stacked pin-fed patch is straightforward to construct and avoids feed network radiation issues. However, unlike the simple pin-fed rectangular patch, it provides a broader operational bandwidth [32].

The theoretical explanation for why the stacked configuration enhances the bandwidth involves modeling the active antenna as an RLC parallel circuit with a quality factor (Q), which is capacitively coupled to another RLC parallel circuit representing the parasitic patch, characterized by a lower quality factor. To obtain the position of the tight loop full wave simulator has been used. Proper placement of this loop can enhance the bandwidth by up to 10-15% [33]. Electrical model of the stacked patch can be modeled as in Figure 3.1.

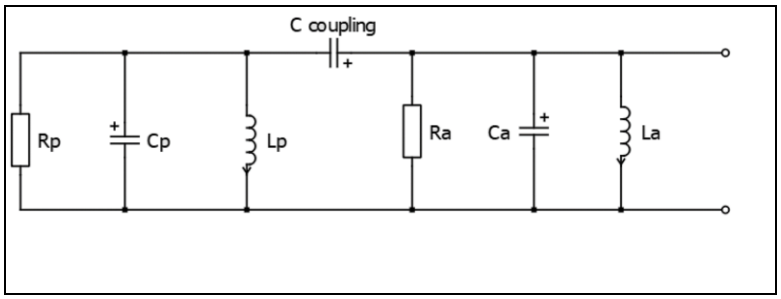


Figure 3.1. Electrical model of stacked patch antenna

Quality factor of the parasitic element is given by

$$Q_p = w_0 \cdot R_p \cdot C_p \tag{3.1}$$

Quality factor of the active element is given by

$$Q_a = w_o \cdot R_a \cdot C_a \tag{3.2}$$

Total quality factor of the stacked patch antenna model is given by the combination of both quality factors.

$$Q_t^{-1} = Q_p^{-1} + Q_a^{-1} \approx Q_p^{-1} \tag{3.3}$$

From this it is evident that parasitic patch gives the antenna a broader bandwidth because of its distance from the ground plane. A single layer patch antenna with the same thickness would achieve a similar bandwidth to this type of antenna, but it would exhibit poorer radiation pattern due to travelling wave phenomenon [34]. With stacked patch antennas this phenomenon is avoided due to active patch being near the ground plane, therefore maximum gain is in the broadside direction.

Figure 3.2. and Figure 3.3. shows the cross section of the designed probe-fed rectangular patch antenna with different views. It can be seen that bottom of the patch is fed by a coaxial probe through the ground plane. Outer conductor of coaxial probe is connected to the ground plane. Inner conductor reaches and connects to the bottom patch. The feed point is positioned to control the input impedance of the antenna which is 50Ω in this design. To analyze the position of the probe accurately full wave simulations are conducted based on time domain method.

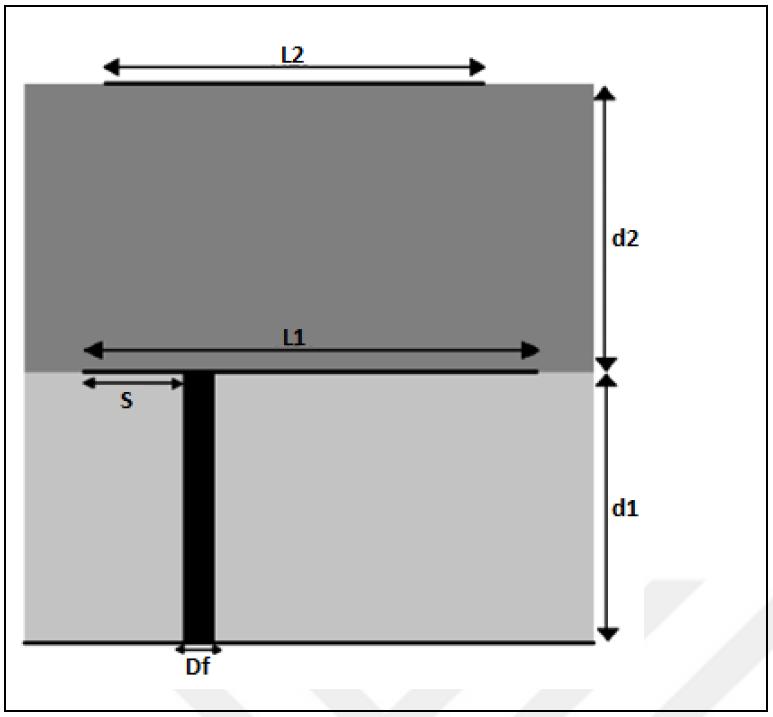


Figure 3.2. Cross section side view

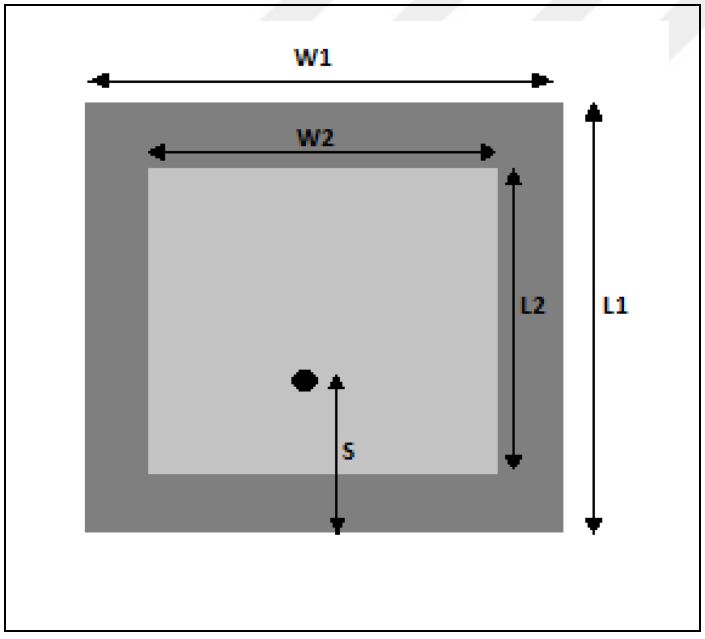


Figure 3.3. Cross section top view (dielectric not visible)

There are very few or basically no analytical equations to design this type of antenna. It is designed through trial and error. Initial design parameters are found and optimized from this starting point through full wave simulator. Bandwidth (BW) of the antenna is found to be the best when d1 and d2 values were approximately $0.025\lambda_0$. The thickness of the substrates controls the tightness of the resonant loop. Both of the substrates have identical

materials with ε_{r_1}= 3.35 and tanδ = 0.001. It is more convenient to initially select the dielectric constant (ε) and subsequently adjust other parameters such as patch size, dielectric thickness, and probe location to fine-tune the antenna for broadband behavior. This method allows for a systematic optimization process, where fixing the primary material property (dielectric constant) simplifies the subsequent modifications required to achieve the desired impedance bandwidth. A good starting point for determining the dimensions of the rectangular patches is to use a length approximately equal to half of the guided wavelength ($\lambda_g/2$), λ_g is the guided wavelength in the bottom layer substrate material [32]. In this configuration, the centers of both patches are aligned. The RF energy is transferred from the bottom patch to the upper patch through coupling capacitance. The dimensions of the second patch and the substrates are crucial because effective coupling between the patches leads to increased bandwidth and gain [35]. However, if the coupling between the patches is too strong patches will have different resonant frequencies. On the other hand, if the coupling is too weak, the bandwidth will be narrower. The effect of parameters on input impedance and effect on the antenna performance are given in Table 3.1.

Table 3.1. Effect of dimensions on the antenna element performance

Parameter	Overall Effect
L_1↑	Significant change in input impedance
L_2↑	Significant change in input impedance
d2 ↑	Bandwidth ↑
L_1, L_2 ↑	Frequency of operation ↓
W1 ↓	Bandwidth ↓
W2 ↓	Minor change
ε_{r_2}↑	Coupling↑

Dimensions and dielectric constant values of the designed antenna are given in Table 3.2.

Table 3.2. Antenna element parameter values

Parameter	Value
ε_{r_1}	3.35
ε_{r_2}	3.35
L1, W1	7.29 mm

Table 3.2. (Continued) Antenna element parameter values

L2, W2	7.37 mm
S	3.55 mm
Df	0.6 mm
d1	0.74 mm
d2	0.77 mm

A broadband compact antenna using the above parameters has been designed with CST microwave studio software and simulated using time domain method. The 3D model of the antenna element is given in Figure 3.4.

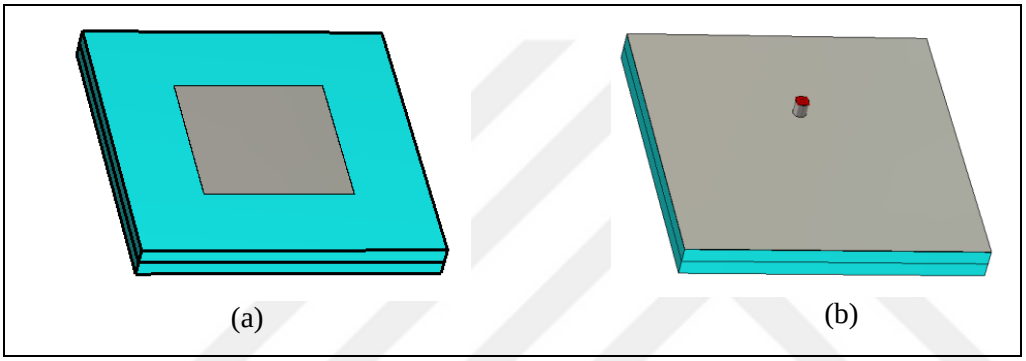


Figure 3.4. Patch antenna 3D model (a) Top view (b) Bottom view

Simulated return loss characteristics are shown in Figure 3.5. The occurrence of two resonance frequencies arises from the different resonances of the patches. When the coupling between these patches is appropriate, it shows broadband response characteristics. However, if the coupling between patches is too strong, the broadband behavior is replaced by a dual-band response, characterized by two separate resonance frequencies. Conversely, if the coupling is too weak, the interaction between the patches is insufficient to sustain the second resonance, causing it to disappear entirely [35]. Therefore, achieving the desired broadband performance depends on optimizing the coupling strength between the patches to maintain both resonances effectively. The limiting factor for bandwidth performance is the size of the antenna element. Increasing the dimensions of the patch, higher bandwidth can be achieved but at the cost of impedance control. However, our design goal is to create an element small enough to maintain an inter-element spacing of $\lambda/2$ in the array.

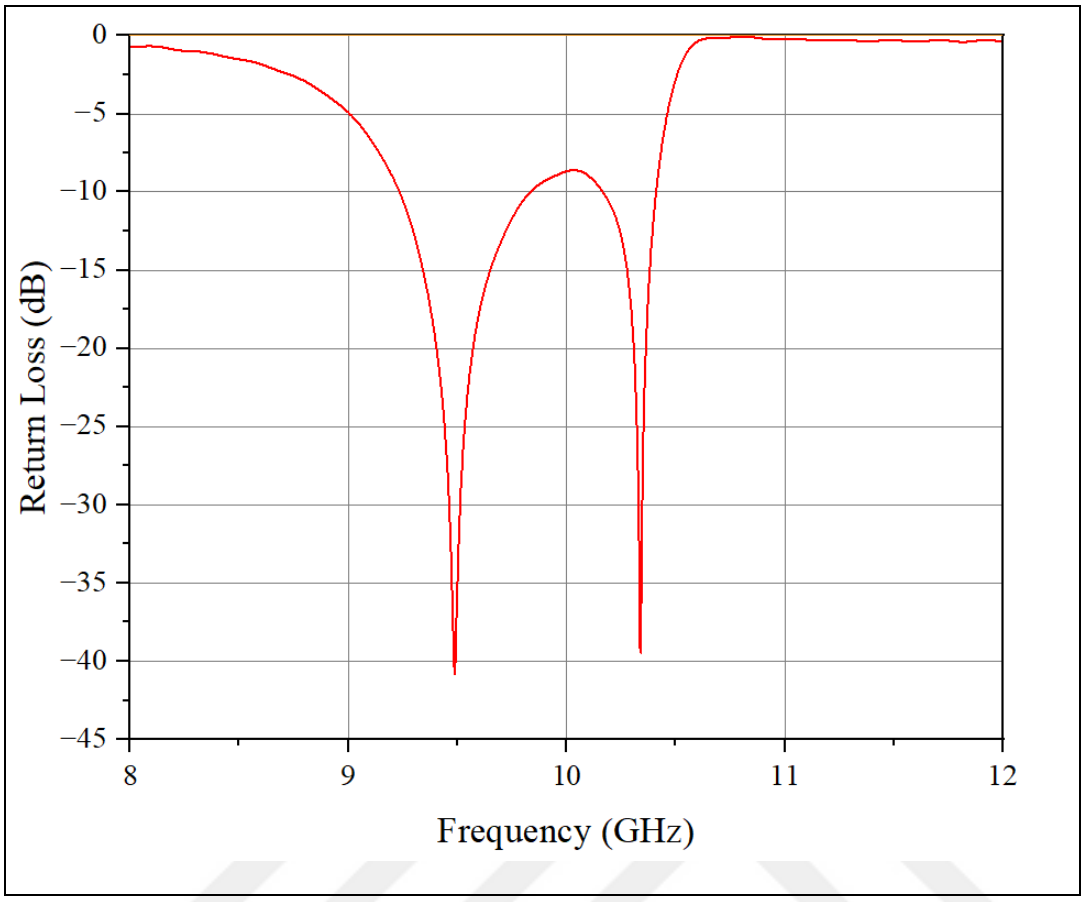


Figure 3.5. Return Loss S_{11} Plot

In Figure 3.6. the simulated maximum broadside gain of the designed antenna over the frequency range in the X band is presented. The maximum gain observed is 6.82 dBi at 10.3 GHz. Within the matching band, which spans from 9.23 GHz to 10.41 GHz, the gain ranges from 6.26 dBi to 6.82 dBi. This indicates a consistent performance across the operating bandwidth, ensuring that the antenna maintains a relatively high gain within this frequency range.

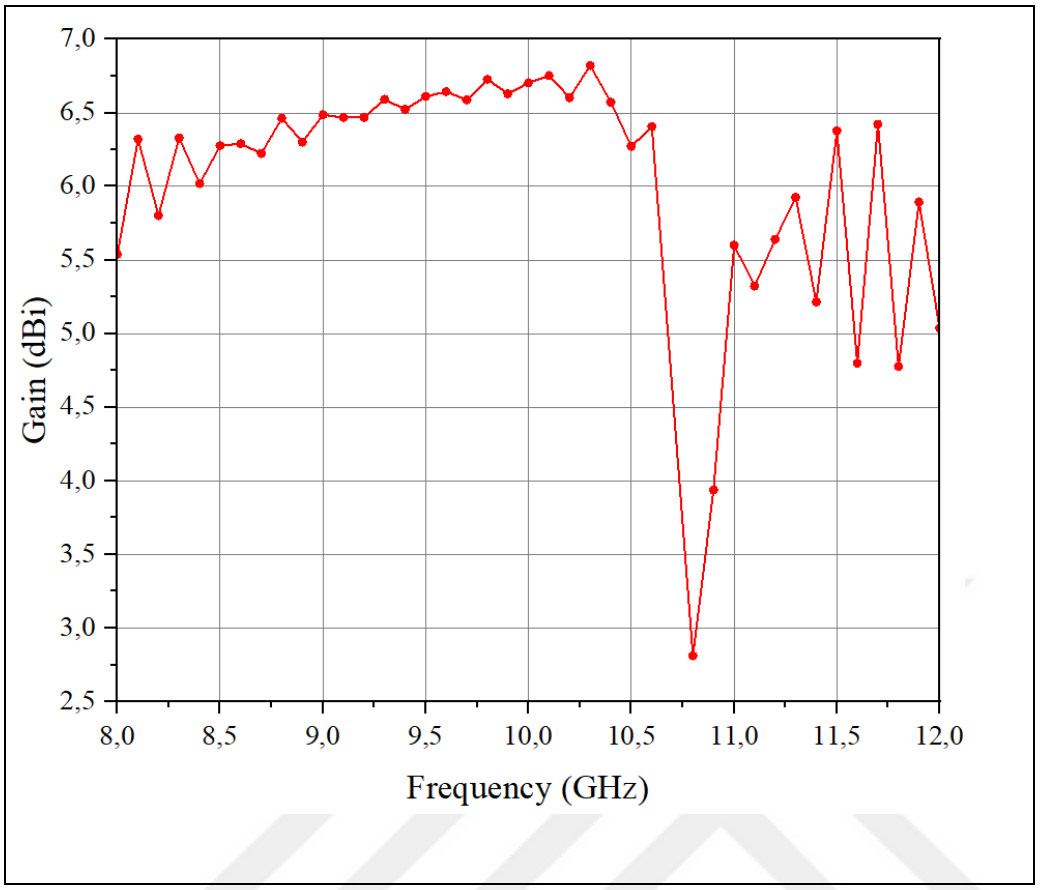
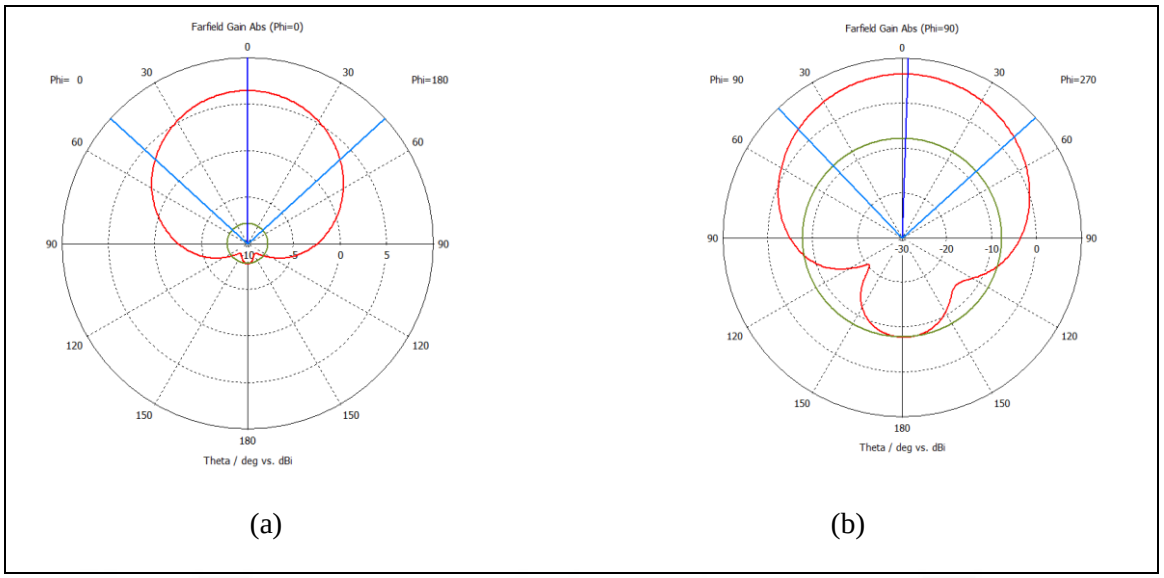


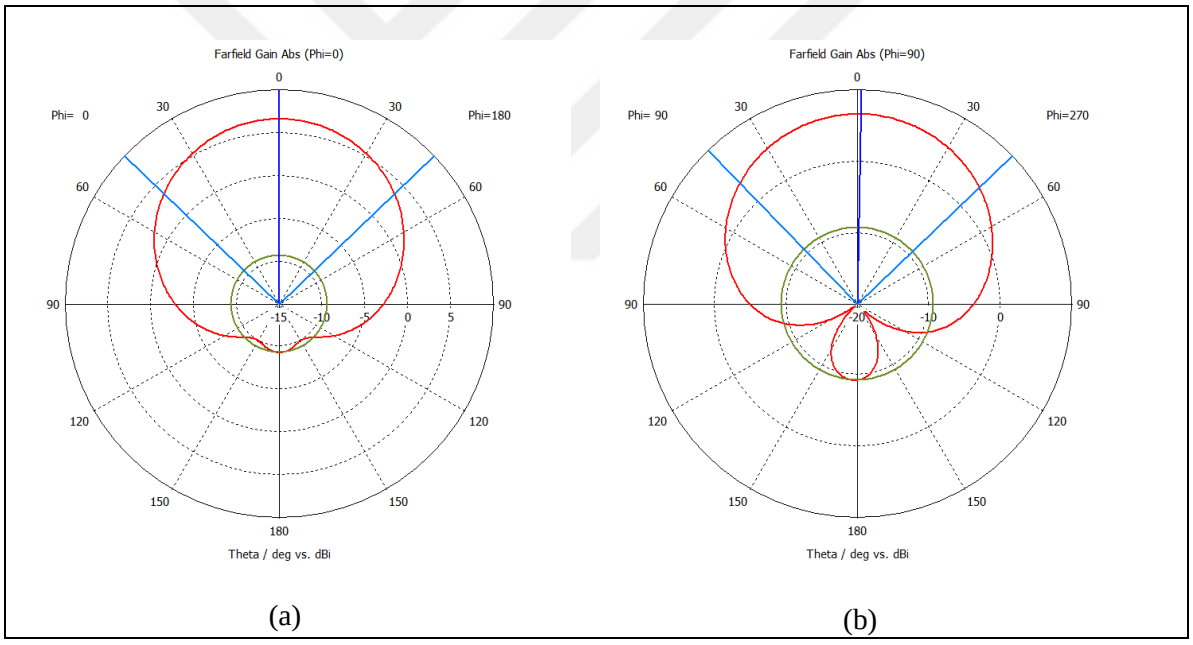
Figure 3.6. Maximum Gain vs Frequency

The co-polarization radiation pattern polar plots of the antenna at frequencies 9 GHz, 9.5 GHz, 10 GHz, and 10.5 GHz are illustrated in Figure 3.7. through Figure 3.10. for both planes. It is observed that the maximum gain of the cross-polarization component is 26.07 dB lower than that of the co-polarization component at 10 GHz, as shown in Figure 3.11. This significant cross polarization isolation indicates that the antenna effectively minimizes cross-polarization interference, thus enhancing the overall polarization purity. Additionally, the antenna exhibits good directionality, which is crucial for fire control radar applications. The simulated 3D radiation pattern of the antenna element is given in Figure 3.12.



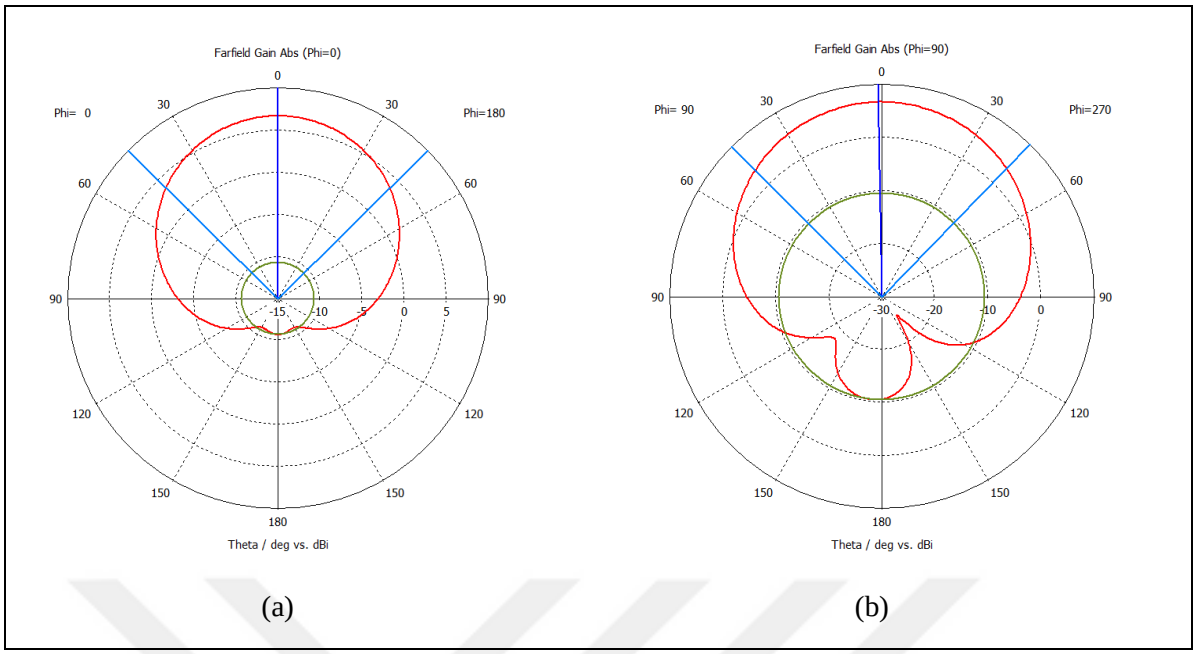
(a) (b)

Figure 3.7. f=9 GHz radiation pattern polar plot (a) $\phi = 0$ (b) $\phi = 90$



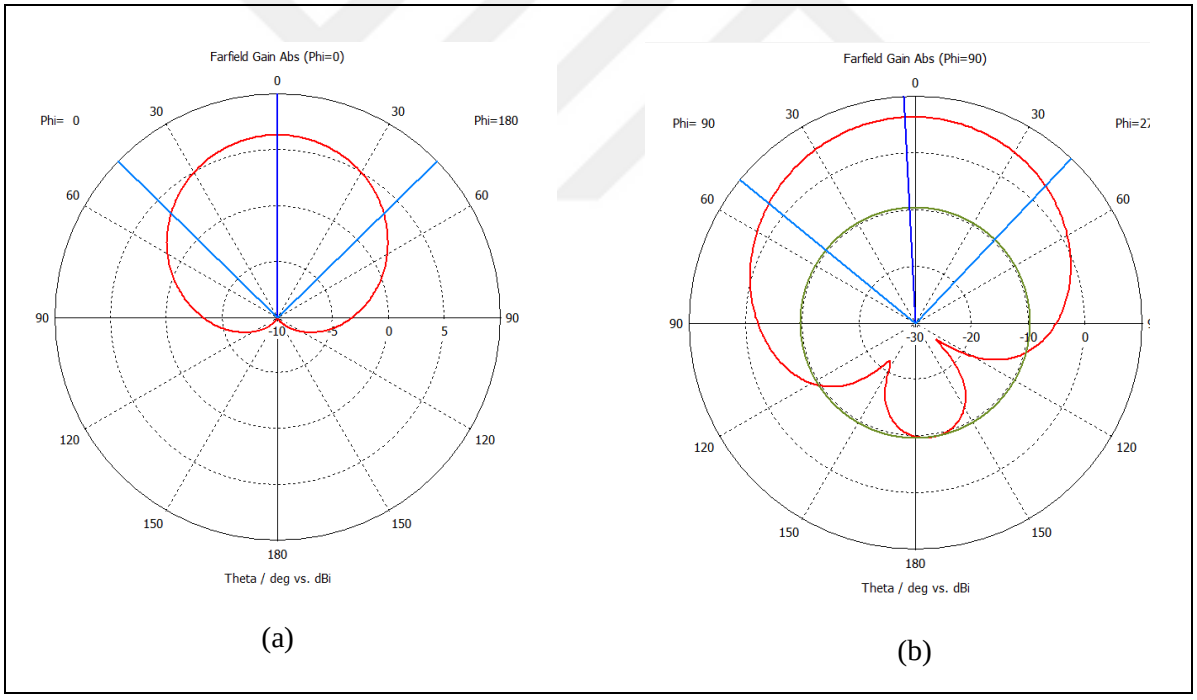
(a) (b)

Figure 3.8. f=9.5 GHz radiation pattern polar plot (a) $\phi = 0$ (b) $\phi = 90$



(a) (b)

Figure 3.9. f=10 GHz radiation pattern polar plot (a) $\phi = 0$ (b) $\phi = 90$



(a) (b)

Figure 3.10. f=10.5 GHz radiation pattern polar plot (a) $\phi = 0$ (b) $\phi = 90$

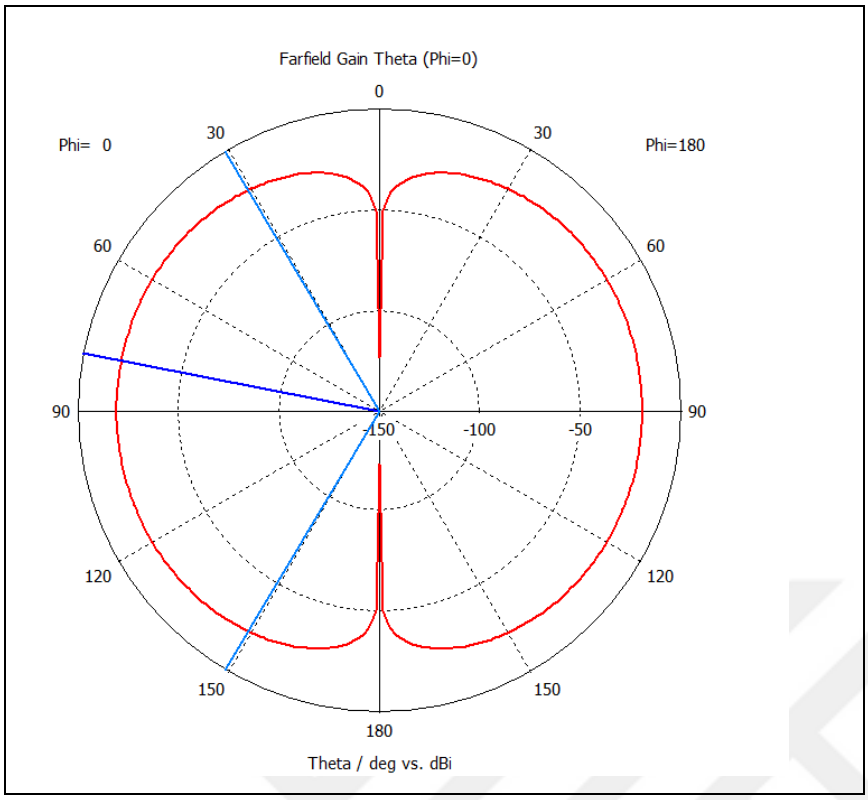


Figure 3.11. Cross-polarization pattern at f=10 GHz ($\phi = 0$)

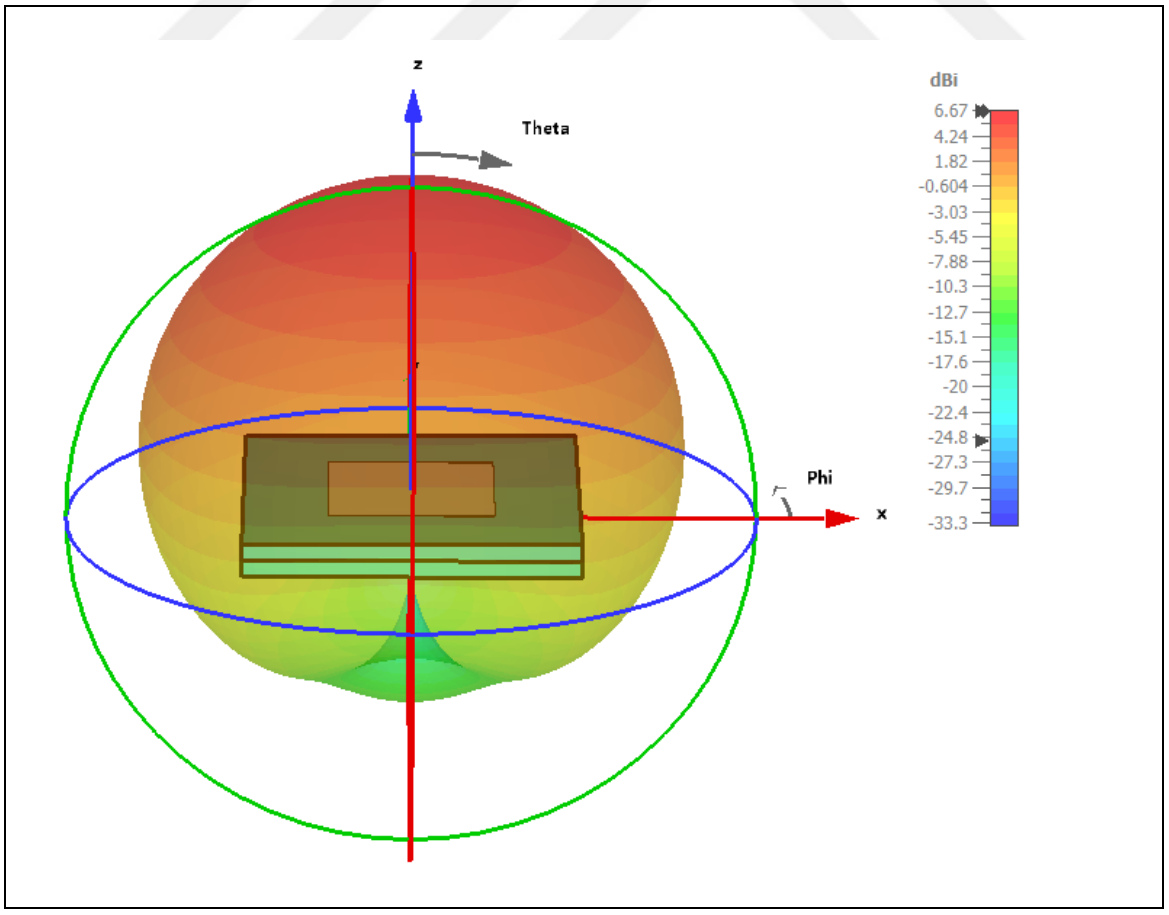


Figure 3.12. 3D radiation pattern at f=10 GHz

3.2. Unit Cell Design

The second stage of the design involved creating an underside microstrip corporate feed for a smaller array, referred to as the unit cell. This unit cell design was necessary to simulate the effect of transmission loss in the T/R modules on the antenna mode RCS. The unit cell consists of 16 patch antenna elements fed by a single input. Mitered sections are employed at 90-degree corners and T-junctions to minimize mismatch caused by reflections at discontinuities. Quarter-wave transformers are used to achieve impedance matching.

The array operating frequency range does not totally depend on antenna element itself. Transmission line plays a huge part on frequency response of the system. Efficient matching network is necessary to couple the antenna element and transmission line for optimum performance [31]. There are many matching techniques that are available to couple the antenna element to the transmission line for achieving good frequency response. Quarter wave transformer technique is one of them. Quarter-wave transformer technique is useful for microstrip based array applications due to ease of controlling the impedance of the microstrip line. The impedance of the antenna element in practice is complex whereas transmission line impedance is real. Therefore, the transformer is placed at a distance s_0 from the antenna. s_0 is chosen because input impedance toward the load is real and is designated as R_{in} [16]. Model for the transformer is shown in Figure 3.13. For impedance matching, impedance of the transformer should be $Z_q = \sqrt{R_{in}Z_0}$, where Z_0 is the characteristic impedance of the transmission line, in our case it is 50Ω.

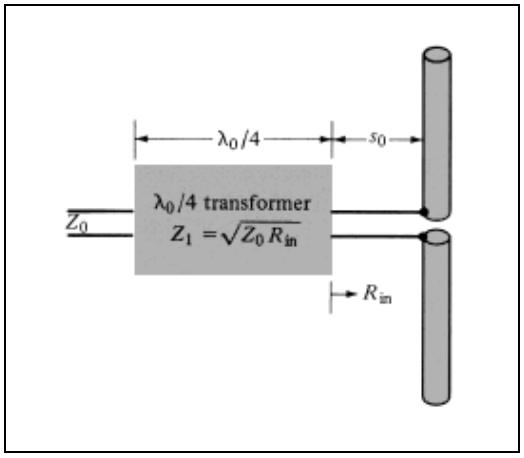


Figure 3.13. Quarter wave transformer [16]

The transformer is another microstrip transmission line. Microstrip transmission line are

suited for array applications. The characteristic impedance of the microstrip transmission line, as shown in Figure 3.14, is given by [36]

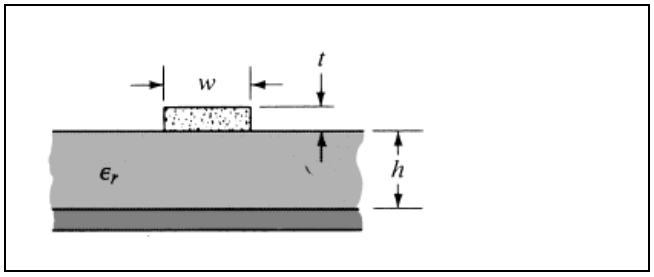


Figure 3.14. Microstrip on a substrate

$$Z_c = \frac{87}{\sqrt{\epsilon_r + 1.41}} \ln\left(\frac{5.98h}{0.8w + t}\right) \qquad \text{,for } h < 0.8w \tag{3.4}$$

Where ϵ_r is the dielectric constant of the substrate, h is the thickness of the substrate, t is the thickness of the microstrip line, w is the width of the microstrip line. Therefore, by varying these parameters desired characteristic impedance can be achieved. In our design following parameters are used to achieve characteristic impedance of 50 ohm.

Table 3.3. Microstrip transmission line parameters.

ϵ_r	3.3
h	0.223 mm
t	0.015 mm
w	0.5 mm

The designed 3D model of the underside corporate feed is shown in Figure 3.15. Inner pin of the antenna element probe is connected to the 50-ohm microstrip lines through the substrate. The impedance of the transformers is calculated as $Z_q = \sqrt{(25) \cdot (50)} = 35{,}35$ ohm. The appropriate trace width for the transformer has been calculated using (3.4).

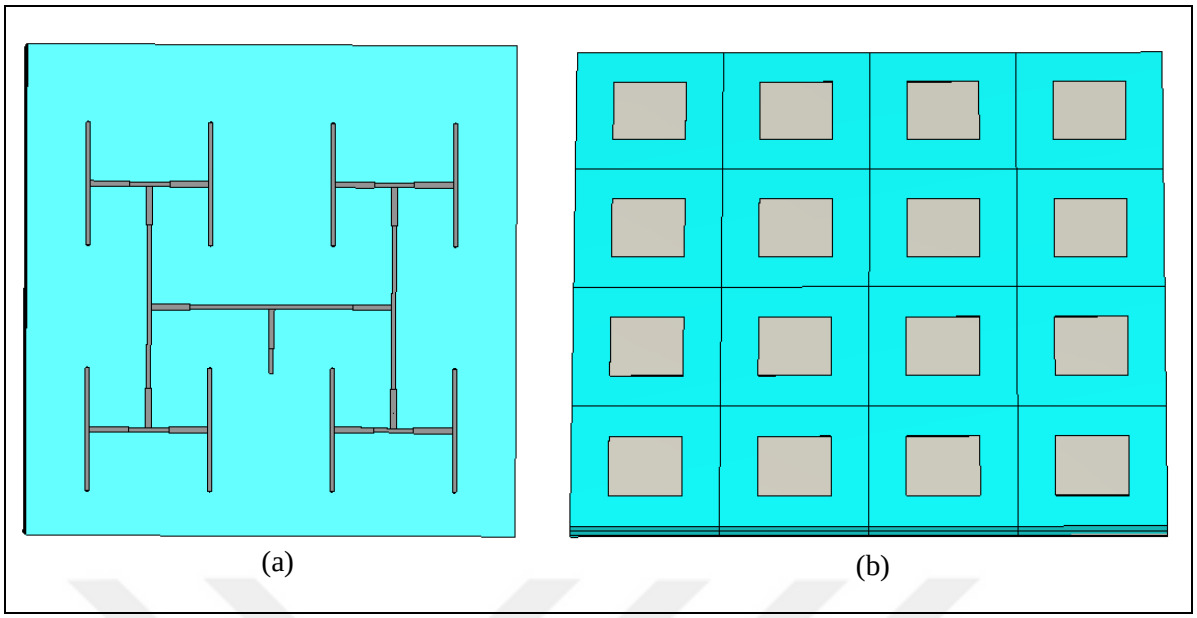


Figure 3.15. Unit cell 3D Model (a) Underside corporate feed (b) Top view

The return loss characteristics of the unit cell are shown in Figure 3.16. The second resonance characteristics of the antenna have changed due to the alteration in the distance from the patch to the load. The –10dB bandwidth of the antenna ranges from 9.21 to 10.3 GHz, which is slightly narrower than the impedance bandwidth of the individual antenna element. RF isolation can be achieved in practice by separating the ground plane of the antenna from the ground plane of the T/R module PCB. This separation helps preserve the bandwidth performance of the antenna element.

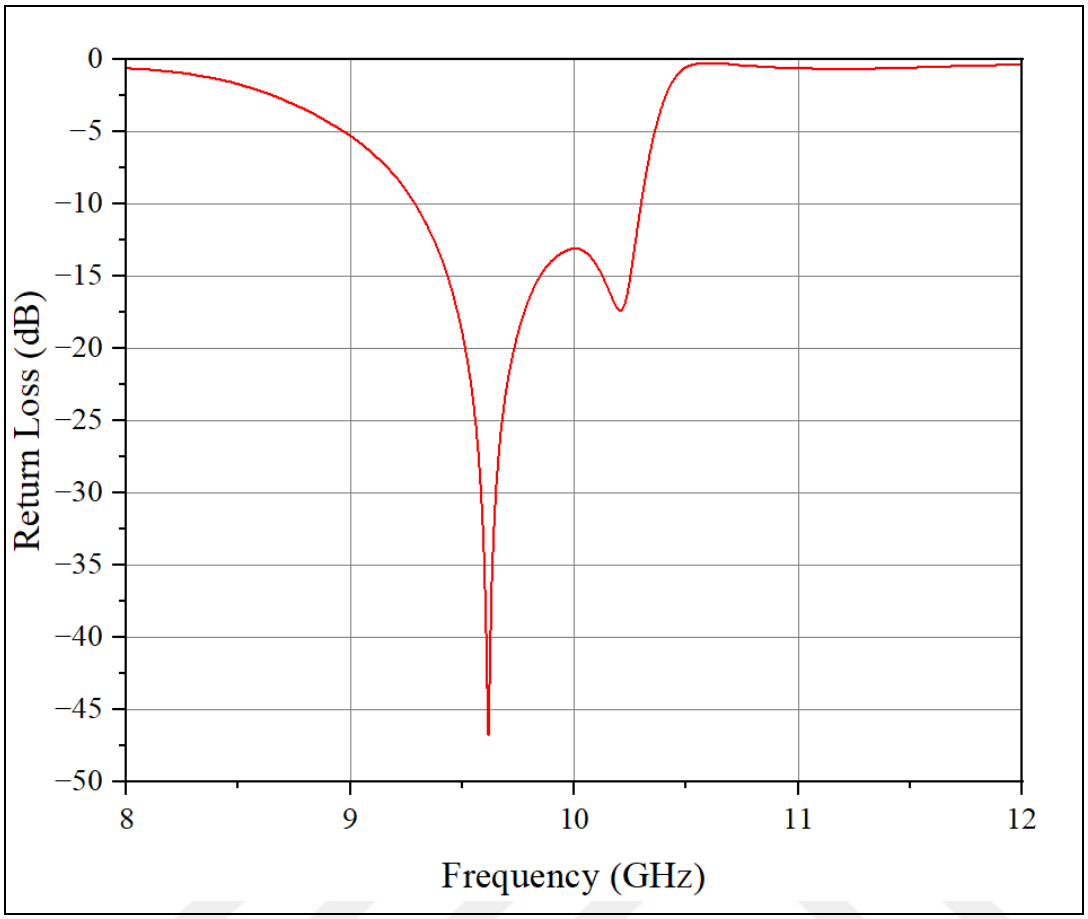


Figure 3.16. Unit cell S11 dB

The maximum broadside gain versus frequency of the unit cell is shown in Figure 3.17. The maximum gain observed is 17.19 dBi at 10.2 GHz. Within the matching band, which spans from 9.21 GHz to 10.3 GHz, the gain ranges from 16.18 dBi to 17.19 dBi. The unit cell design maintains consistent performance within the matching band. The co-polar radiation pattern of the unit cell is given in Figure 3.18. for both planes. The 3 dB beamwidth of the antenna is found to be 25.6 degrees in elevation and 26.2 degrees in azimuth. The first sidelobe level is -12.4 dB in elevation and -14.6 dB in azimuth. The unit cell has a cross-polarization isolation between the H and V patterns of -26.69 dBi.

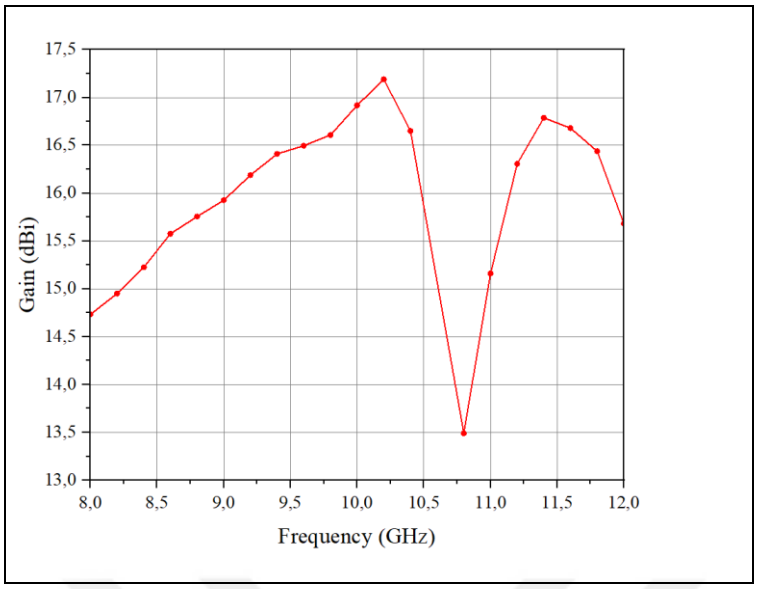
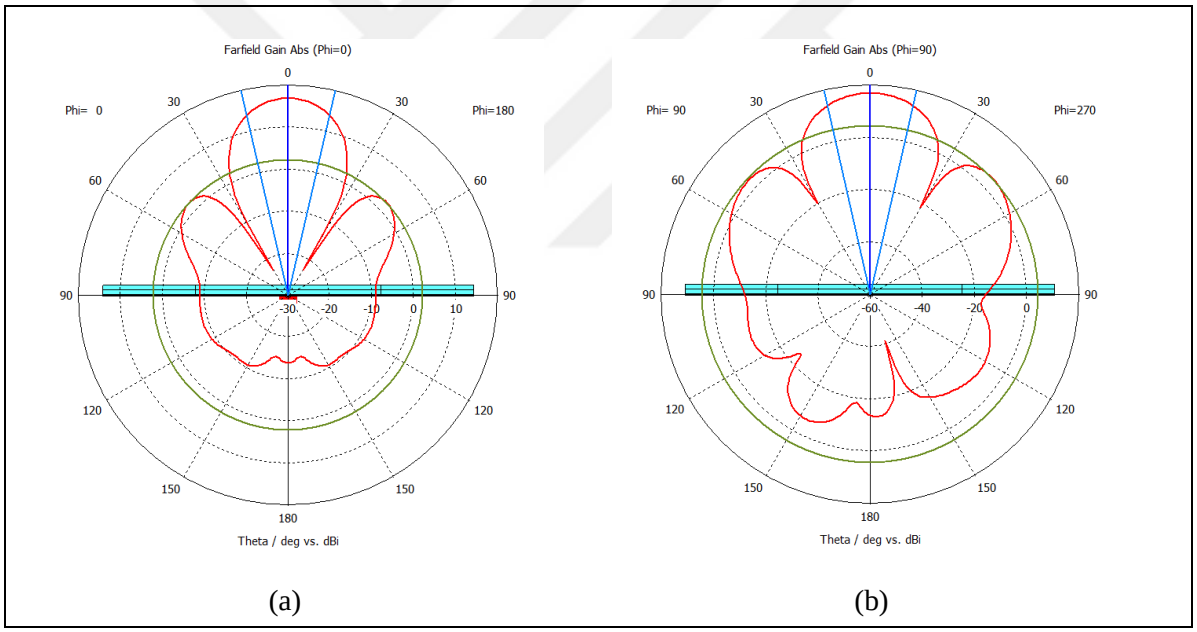


Figure 3.17. Maximum gain over frequency



(a) (b)

Figure 3.18. f=10 GHz radiation pattern polar plot (a) $\phi = 0$ (b) $\phi = 90$

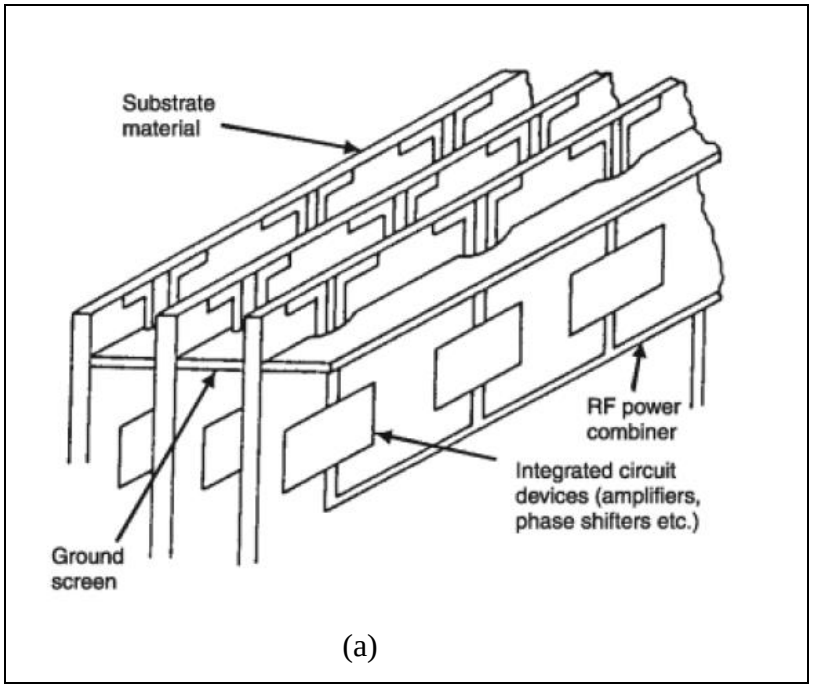
3.3. Phased Array Theory, Design and Analysis

Achieving the substantial advantages of an AESA necessitates meeting numerous strict requirements in its design and implementation. This chapter covers full array architecture considerations, size and geometry determination justifications, array theory, and simulation results.

3.3.1. Array architecture

Designing the AESA antenna begins with determining the array architecture. Two commonly used array constructions in airborne radar systems are the brick and tile configurations [31]. In the brick configuration, the radiating elements are arranged with transmit/receive modules mounted perpendicularly to the array face [37]. This architecture antenna elements generally offers a higher bandwidth compared to microstrip patches. Typical radiating elements for this architecture are flared-notch, dipoles antennas, and many more [31]. However, it requires more volume and is more challenging to implement on older platforms. Figure 3.19. (a) shows the brick construction consisting dipole elements, RF power divider and T/R modules.

On the other hand, the tile architecture is more compact, requiring less space, making it the preferred choice for modernized radar systems, especially when upgrading older platforms. In this configuration, the antenna elements are fed by T/R tile modules that house various electronic components such as low noise amplifiers, power amplifiers, attenuators, phase shifters, and circulators [15]. Figure 3.19. (b) shows the tile construction consisting of RF feed network, microstrip patch radiating elements, electronic control board, monolithic radome.



(a)

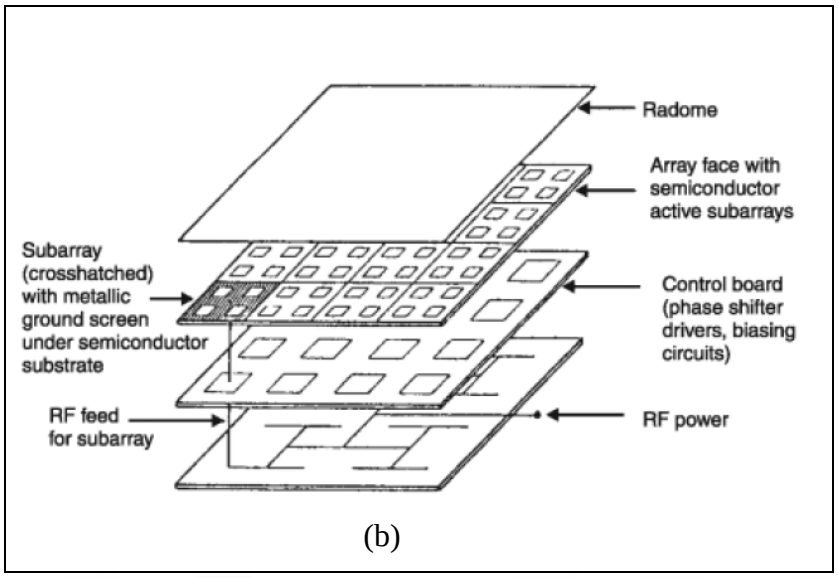


Figure 3.19. Basic array construction types (a) Brick construction dipole array (b) Tile construction microstrip patch array [31]

There are significant challenges in assembling the array and applying element weightings, regardless of whether brick or tile architecture is used. To address these challenges, the array is divided into subarrays, organized into rows or columns for brick architecture, or into areas for tile architecture [31]. Each subarray is fed differently. Beamforming involves combining the outputs of subarrays to generate the necessary sum and difference channels. Figure 3.20. (a) demonstrates a technique for merging subarrays to produce the desired sum and difference patterns. The receive channel may be split into sum, elevation, and azimuth channels, as shown in Figure 3.20. (b). Subarray outputs are weighted and summed for beamforming, which is needed for monopulse angle measurements in receive mode. On transmit all power amplifiers on the T/R modules weighted equally to achieve peak power on the target [1]. Received or transmitted signals are amplified at the subarray level for convenience and improved performance. This approach allows for more efficient signal processing within each subarray, ensuring that the signals are at optimal levels before being combined for further analysis or transmission [18]. In receive mode, amplitude tapering can be employed to subarrays to reduce sidelobe levels. Aperture taper is used on receive mode only in order to suppress ground clutter or other unwanted signals [38].

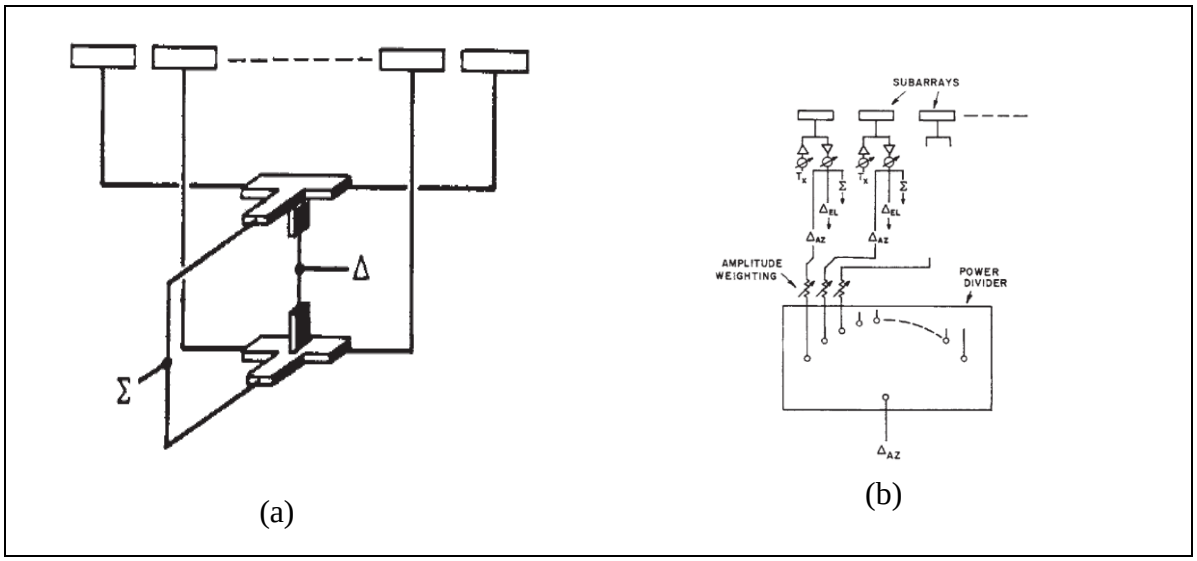


Figure 3.20. Combining of subarray channels (a) Combining subarrays to sum and difference channels (b) The receiving channel split into azimuth, elevation and sum channels [1]

3.3.2. Phase scanning for planar arrays

If we consider a planar array with M elements in x axis and N elements in y axis of Figure 3.20. with elements defined with [31]

$$r_{m,n} = \hat{x}md_x + \hat{y}nd_y \tag{3.5}$$

Where, d_x and d_y are the spacing between elements in x and y direction respectively,

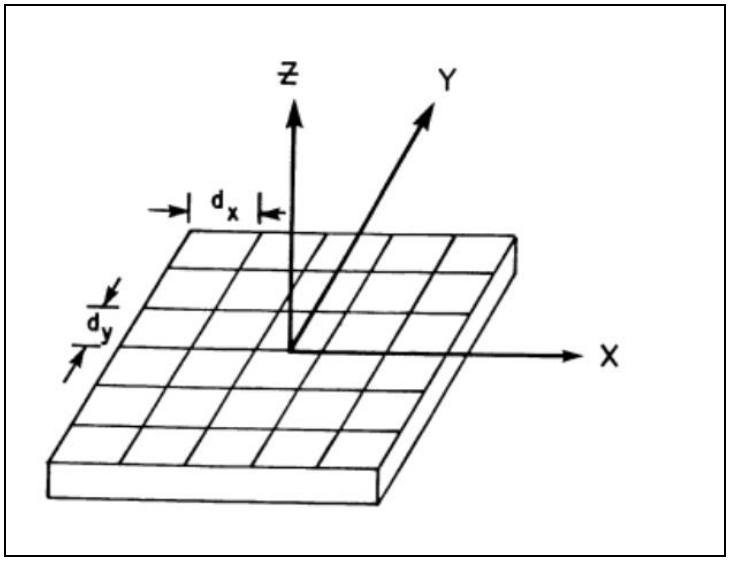


Figure 3.20. Planar array geometry [31]

Array factor with peak beam steered to with phase steering at frequency f_0 would be given by the following equation [16].

$$F(\theta,\phi) = \sum_{n=1}^{N} I_{1n} \left[\sum_{m=1}^{M} I_{m1} e^{j(m-1)(kd_x \sin\theta\cos\phi+\beta_x)} \right] e^{j(n-1)(kd_y \sin\theta\sin\phi+\beta_y)} \tag{3.6}$$

Where M is the number of elements in the x-axis, N is the number of elements in the y-axis, I_{1n} and I_{m1} are excitation coefficients, dx and dy are spacing between elements in x-axis and y-axis respectively, β progressive phase shift between the elements, θ and ϕ are the look direction and, k constant is

$$k = \frac{2\pi}{\lambda_0} \tag{3.7}$$

Planar array pattern can be written as product of array factors of the arrays in x-axis and y-axis

$$F(\theta,\phi) = S_{xm} S_{yn} \tag{3.8}$$

Where;

$$S_{xm} = \sum_{m=1}^{M} I_{m1} e^{j(m-1)(kd_x \sin\theta\cos\phi+\beta_x)} \tag{3.9}$$

$$S_{yn} = \sum_{n=1}^{N} I_{1n} e^{j(n-1)(kd_y \sin\theta\sin\phi+\beta_y)} \tag{3.10}$$

For rectangular array aperture amplitude weighting is separated as

$$I_{mn} = I_{m1} I_{1n} \tag{3.11}$$

If amplitude weighting is uniform across the array, i.e. $I_{mn} = I_0$

$$F(\theta,\phi) = I_0 \sum_{m=1}^{M} e^{j(m-1)(kd_x \sin\theta\cos\phi+\beta_x)} \sum_{n=1}^{N} e^{j(n-1)\left(kd_y \sin\theta\sin\phi+\beta_y\right)} \tag{3.12}$$

If the desired look direction is at $\theta = \theta_0$ and $\phi = \phi_0$, the progressive phase shift between the element is calculated as

$$\beta_x = -kd_x \sin\theta_0 \cos\phi_0 \tag{3.13}$$

$$\beta_y = -kd_y \sin\theta_0 \sin\phi_0 \tag{3.14}$$

A planar array with its peak beam at (θ, ϕ) can have other peak values depend on the interelement spacing. When the spacing between antenna elements is equal to or larger than λ/2, multiple beam peaks can exist. These peaks are called grating lobes and are defined as the lobes that appear beside the main lobe. To avoid grating lobes for planar arrays in both planes, the spacings d_x and d_y must be less than λ/2 [16].

For planar arrays, main lobe and grating lobes of S_{xm} and S_{yn} are formed at

$$kd_x \sin\theta \cos\phi + \beta_x = \pm 2m\pi \quad \text{, where } m = 0,1,2, \ldots \tag{3.15}$$

$$kd_y \sin\theta \sin\phi + \beta_y = \pm 2n\pi \quad \text{, where } n = 0,1,2, \ldots \tag{3.16}$$

These can be rewritten in terms of β_x and β_y as

$$\phi = \tan^{-1}\left[\frac{\sin\theta_0 \sin\phi_0 \pm n\lambda/d_y}{\sin\theta_0 \cos\phi_0 \pm m\lambda/d_x}\right] \tag{3.17}$$

And

$$\theta = \sin^{-1}\left[\frac{\sin\theta_0 \cos\phi_0 \pm m\lambda/d_x}{\cos\phi}\right] = \sin^{-1}\left[\frac{\sin\theta_0 \sin\phi_0 \pm n\lambda/d_y}{\sin\phi}\right] \tag{3.18}$$

To achieve a 60-degree scan angle without encountering grating lobes, which is a typical scan limit for airborne fire control radar, the array element size must be approximately $0.29\lambda^2$ [31]. In our design, each element occupies an area of about $0.22\lambda^2$.

3.3.3. Element pattern

The array factor defined in previous chapter ignores mutual coupling effects between array

elements and expresses array radiation pattern by pattern multiplication method which is the product of array factor and element pattern. The element pattern is assumed to be same for every element in the array. When two antenna elements are closely placed each other, part of the energy ends up on the other element. The magnitude of this coupling between the elements is related to spacing between the elements, radiation characteristics of elements, and the orientation between them. In large array antennas the coupling between the elements is quite strong so the element pattern and impedance of each element is varied. This effect due to energy exchange is called mutual coupling and it is difficult to estimate analytically. Active element pattern is defined as the pattern obtained from a single element in the array environment while other elements are terminated with matched loads. This pattern is different from the isolated element pattern due to mutual coupling. The radiation pattern of an active element changes from one element to another. However, in larger arrays, all elements have similar radiation characteristics. Consequently, the central element is often considered to have a typical impedance representative of the entire array, as it is most influenced by the surrounding elements [31].

For large arrays, if it is assumed that all elements have the same element pattern of [39]

$$G_e(\theta_o, \phi_o) = \frac{4\pi d_x d_y}{\lambda^2} \cos\theta_0 \tag{3.19}$$

The maximum gain when a N element planar array is scanned to the angle (θ_0, ϕ_0) is

$$G^{max}(\theta_o, \phi_o) = \frac{4\pi d_x d_y}{\lambda^2} N \cos\theta_o \tag{3.20}$$

The realized gain of the full array that accounts for reflection loss $\Gamma(\theta_o, \phi_o)$ is

$$G(\theta_o, \phi_o) = \frac{4\pi d_x d_y}{\lambda^2} N[1 - |\Gamma(\theta_o, \phi_o)|^2]\cos\theta_o \tag{3.21}$$

This derivation assumes all elements have the same reflection coefficient. Gain of the active element $G^e(\theta, \phi)$ is defined as the singly excited element while other antenna elements of the array terminated with matched load. By superposition of the element patterns the gain of the full array scanned to the angle (θ_0, ϕ_0) is

$$G(\theta_o, \phi_o) = NG^e(\theta_o, \phi_o) \quad (3.22)$$

This derivation shows that full array gain is proportional to the active element pattern at the same look angle. Therefore, full array radiation pattern will have similar characteristics to active element pattern. This derivation is only useful when an isolated type array feed like corporate feed is utilized. If series type feed is used in the array active element pattern would not be applicable due to multiple reflections on the feed line [31].

3.3.4. Taylor pattern synthesis

Pattern synthesis is a major advantage of array antennas to find the proper weight distribution to produce low sidelobe patterns or to produce desired radiation patterns. Many array synthesis methods have been developed and they fit into three classes: low sidelobe pattern synthesis; narrow beam patterns, and synthesis of sector patterns with a specified beam width. Low sidelobe pattern synthesis is desirable for radars on receive phase due to avoid false target detection and ground clutter, etc. Pattern synthesis is not preferred on transmit phase due to reduction of resolution and lower peak power because of drops in antenna gain and beamwidth increase [31].

The Taylor synthesis is one of the most popular synthesis methods for designing low sidelobe arrays. Developed as a realizable form of the Chebyshev pattern method, it diverges in key aspects to enhance practical applicability and performance. Unlike the Chebyshev method, which produces a pattern with constant sidelobe levels, the Taylor synthesis creates a pattern where sidelobes are uniform near the main beam but decrease in level further from the main lobe, enhancing overall efficiency. This approach balances sidelobe suppression and beamwidth control, reducing power wasted in higher-order sidelobes. The Taylor synthesis allows for flexible adjustment between beamwidth and sidelobe levels, making it valuable in applications where both low sidelobes and controlled beamwidth are crucial [31].

Taylor source distribution is given by [16];

$$I_n(z') = \begin{cases} J_0\left[j\pi B\sqrt{1-\left(\frac{2z'}{l}\right)^2}\right] & -l/2 \le z' \le +l/2 \\ 0 & \text{elsewhere} \end{cases} \quad (3.23)$$

Where J_0 is the Bessel function of the first kind of order zero, l denotes the total length of the continuous source, and B is a constant that is determined based on the specified sidelobe level, z' is the element position. Space factor is defined as array factor for continuous distribution. Space Factor (SF) for Taylor distribution line-source is given by

$$\mathrm{SF}(\theta) = \begin{cases} l\frac{\sinh[\sqrt{(\pi B)^2 - u^2}]}{\sqrt{(\pi B)^2 - u^2}}, & u^2 < (\pi B)^2 \\ l\frac{\sin[\sqrt{u^2 - (\pi B)^2}]}{\sqrt{u^2 - (\pi B)^2}}, & u^2 > (\pi B)^2 \end{cases} \quad (3.24)$$

Where;

$$u = \frac{\pi}{\lambda} cos\,\vartheta \quad (3.25)$$

The constant B can be found from

$$R_0 = \frac{1}{0.217233}\frac{\sinh(\pi B)}{\pi B} = 4.603\frac{\sinh(\pi B)}{\pi B} \quad (3.26)$$

Where R_0 is the intensity ratio found when major-to-the-sidelobe level is specified. Values of B for typical values of sidelobe levels are shown in Table 3.4. below.

Table 3.4. Values of constant B for specified side lobe Level (SLL).

Sidelobe Level (dB)	−10	−15	−20	−25	−30	−35	−40
B	j0.4597	0.3558	0.7386	1.0229	1.2761	1.5136	1.7415

3.3.5. Array design and analysis

An array with 1200 elements has been designed using antenna elements in Section 3.1 and

shown in Figure 3.21. The aperture size and geometry of the array are determined to fit the F-16 fighter jet. The width and length of the array are 649.2 mm and 531.2 mm, respectively.

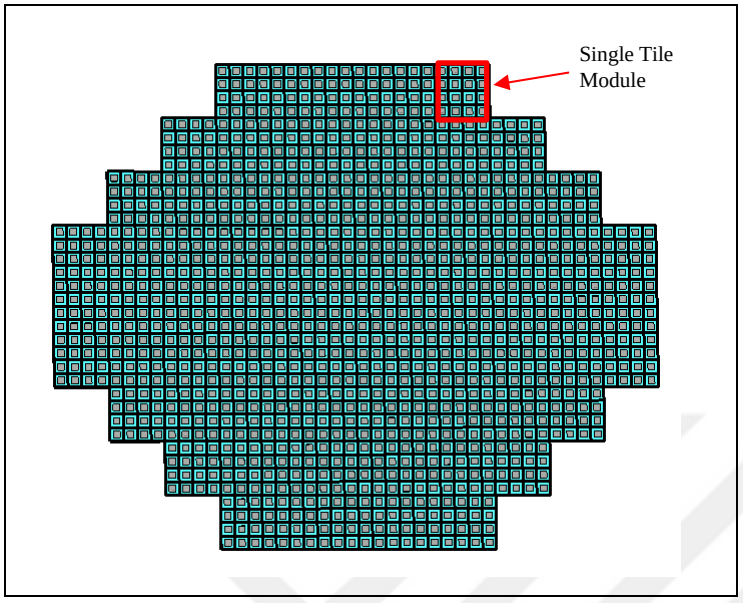


Figure 3.21. Full array model consisting of 75 AESA modules with each module containing 16 antenna elements

The array employs tile construction, utilizing stacked microstrip patch antennas as the array elements. This choice is driven by their compact size, relatively broad bandwidth, and moderate gain characteristics. The rectangular stacked microstrip patch antenna was selected specifically for its size, ensuring that the spacing between elements is equal to or less than half the wavelength (λ/2). Therefore, the occurrence of grating lobes in the radiation pattern is prevented.

The computation of the array radiation pattern using the aforementioned pattern multiplication method does not account for mutual coupling effects on the radiation pattern and is not entirely accurate for analyzing large arrays. Consequently, a full-wave simulation was conducted to analyze the array's performance, which was later compared with the pattern multiplication results. The more accurate active element pattern method mentioned earlier was not utilized due to its limitations, such as assuming uniform element patterns across all elements.

In the simulation runs, the active element S11, radiation pattern, and scanning performance of the array are investigated. The time-domain solver of CST is employed for these

simulations due to its efficiency in handling large objects. It utilizes the Conformal Perfect Boundary Approximation (PBA) conformal meshing approach, which ensures high accuracy in simulating complex structures. The Finite Element Method (FEM) is considered impractical due to its resource-intensive nature and time-consuming computations, especially given the size of the structure [40].

The simulated co-polarization radiation pattern in xz cut at different frequencies of the full array is shown in Figure 3.22. All the ports are uniformly illuminated for this simulation run. At 10 GHz main lobe magnitude is 35.75 dBi and the level of the first sidelobe is about -21.7 dB in both planes, The 3-dB beamwidth of the uniformly illuminated array at the broadside main lobe is 2.6 degrees in the azimuth plane and 3.1 degrees in the elevation plane. Antenna beamwidth is crucial for radar performance as it directly impacts both angular resolution and the minimum detectable velocity. A narrower beamwidth enhances angular resolution by allowing the radar to more precisely distinguish between closely spaced targets, providing more accurate directional information. Additionally, a narrower beamwidth focuses the radar energy, increasing the signal-to-noise ratio (SNR). This higher sensitivity helps in detecting smaller velocity changes, therefore effects the minimum detectable velocity. Moreover, a focused beam reduces clutter and interference from unwanted sources, further enhancing the radar's ability to isolate and accurately measure target velocities [31]. The proposed antenna has demonstrated a narrow beamwidth in both planes. Summary of the simulation run at different frequencies are given in Table 3.5.

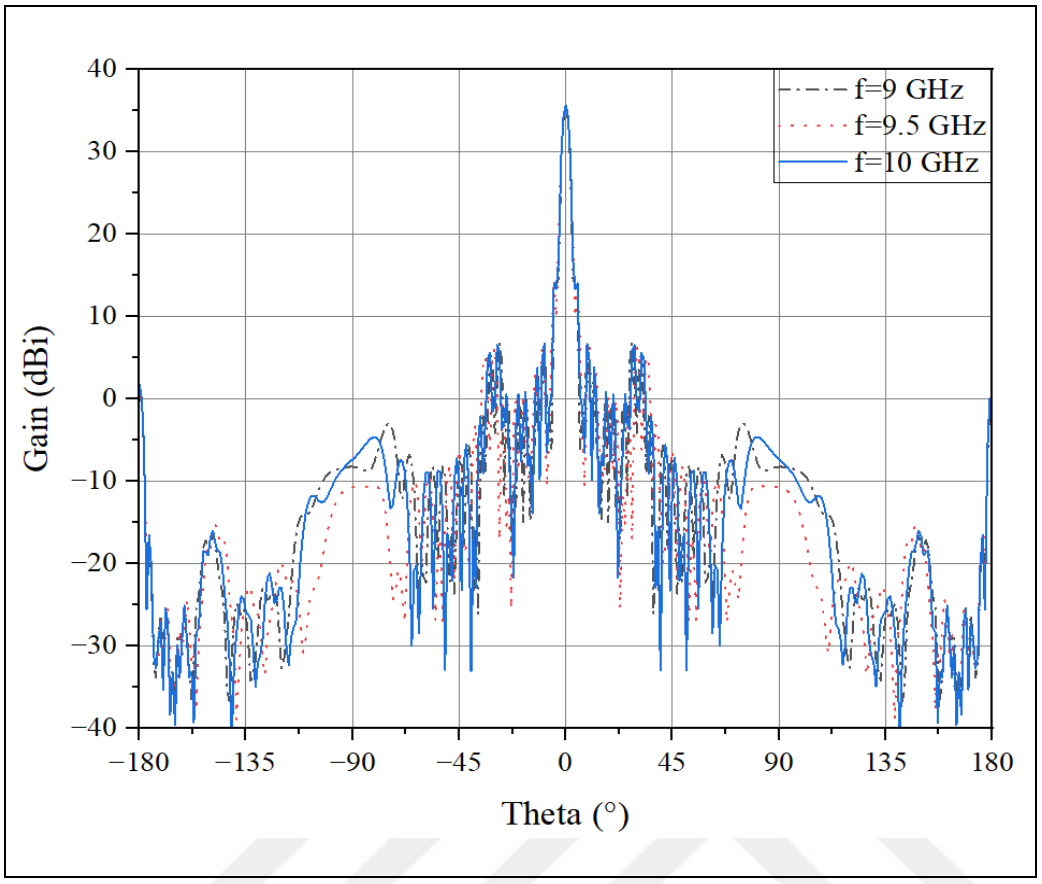


Figure 3.22. Full array radiation pattern at with different frequencies ($\phi = 0$)

Table 3.5. Summary of array radiation pattern (uniform illumination)

Frequency (GHz)	Main lobe magnitude (dBi)	SLL ($\phi = 0$, dB)	SLL ($\phi = 90$, dB)	3-dB beamwidth (degrees, $\phi = 0$)	3-dB beamwidth (degrees, $\phi = 90$)
9	34.7	-20.3	-21.9	2.9	3.6
9,5	35.2	-20.6	-22.9	2.8	3.3
10	35.75	-21.7	-21.8	2.6	3.1

The simulated active element return loss of the central element of the array has been given in Figure 3.23. Inner elements tend to have similar embedded impedance and have similar radiation characteristics. Therefore, central element return loss has been given as a representative of impedance characteristics of the array. In this type of array, only the edge elements have drastically different impedance characteristics and poorer return loss [13] The active element has similar return loss characteristics to the single antenna element shown in Section 3.1 but slightly poorer due to mutual coupling effect.

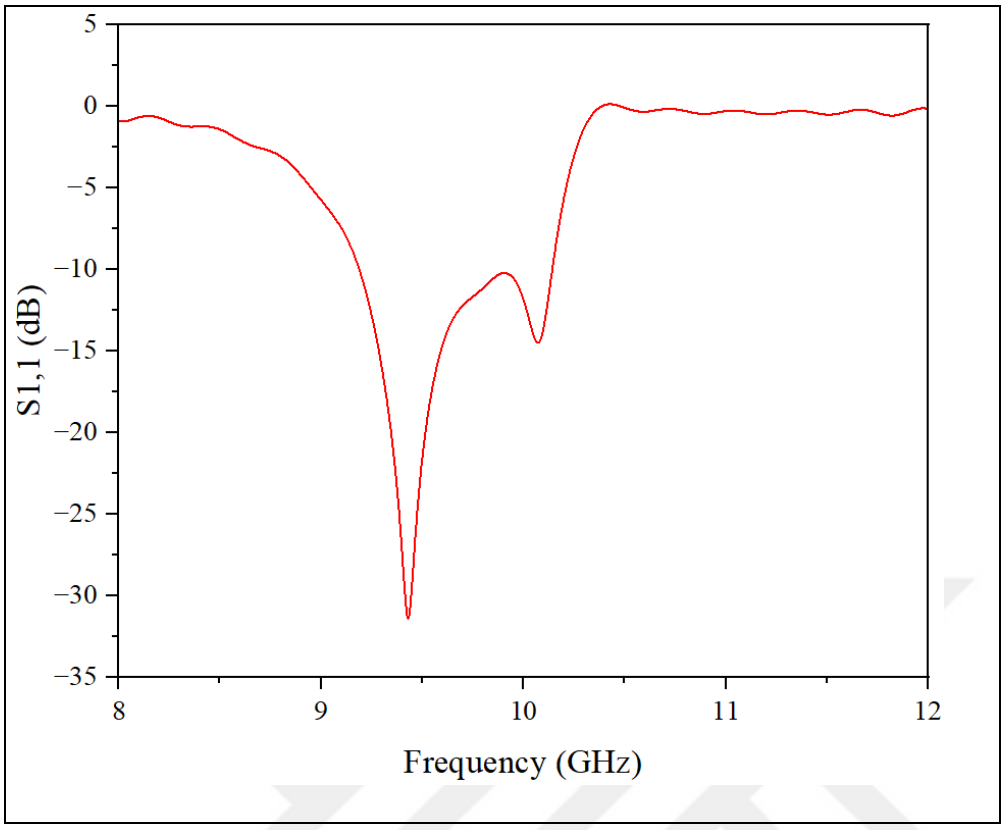
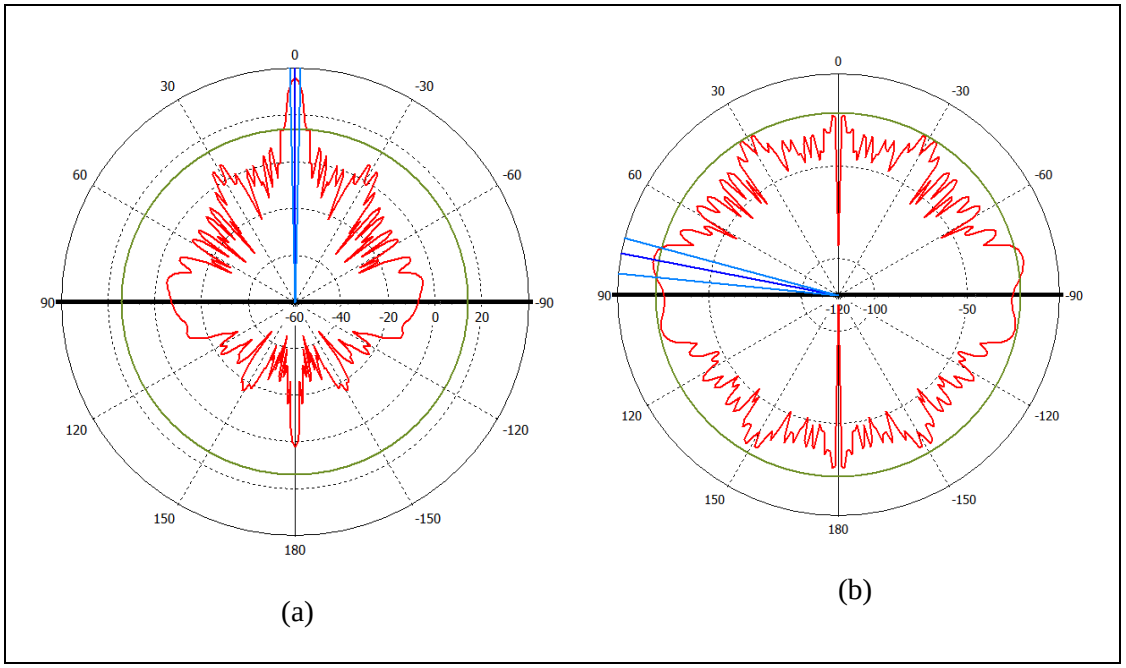


Figure 3.23. Active element return loss.

The simulated radiation patterns of the array in both planes, along with their cross-polarization plots, are shown in Figure 3.24. Results are presented only for 10 GHz to avoid overcrowding the paper. The magnitude of cross-polarization is smaller by 45 dB in both planes compared to co-polarization.



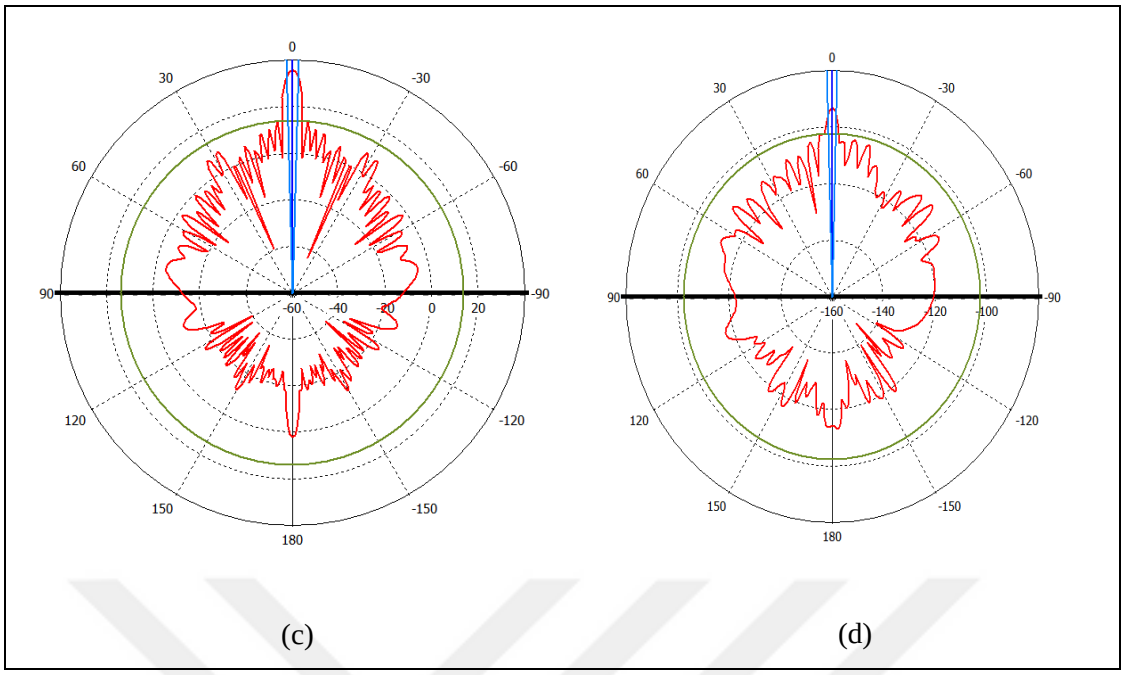


Figure 3.24. Radiation pattern at f=10 GHz (a) $\phi = 0$, co-polar (b) $\phi = 0$, cross-polar (c) $\phi = 90$, co-polar (d) $\phi = 90$, cross-polar

Co-polarization radiation pattern in xz cut with a -30 dB Taylor weighting applied at different frequencies is shown in Figure 3.25. With Taylor weighting, elements at the center excited with higher amplitude than elements close to the edges. Therefore, with Taylor weighting gain of the full array decreases and antenna beamwidth gets wider. At 10 GHz gain magnitude is 34.71 dBi and 3-dB beamwidth in azimuth is 4.28 degrees. As it can be seen from the plot all sidelobes are effectively reduced to below 0 dB at all frequencies.

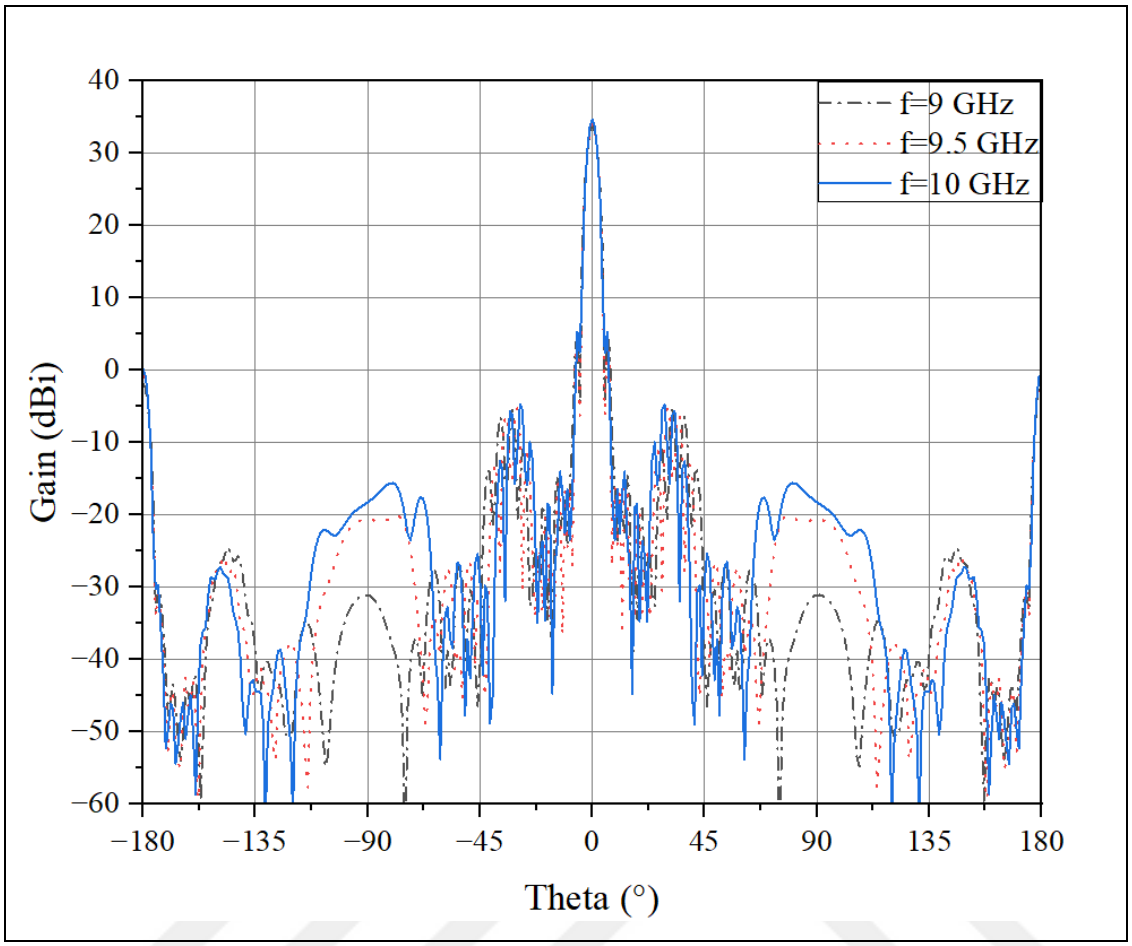


Figure 3.25. Radiation pattern with different frequencies ($\phi = 0$) (With 30 dB SLL Taylor taper)

The CST simulated radiation pattern has been compared with the analytically synthesized radiation pattern at 10 GHz and is shown in Figure 3.26. The synthesized radiation pattern was obtained using the pattern multiplication method mentioned in Section 3.3.2., with the single element pattern shown in Section 3.1. The synthesized pattern has a maximum gain magnitude of 32.78 dBi, with the first sidelobe level being approximately -21.7 dB in the azimuth plane and -21.8 dB in the elevation plane. Although the synthesized maximum gain is approximately 3 dB lower than the simulated one, the sidelobe levels are identical in both cases. The 3-dB beamwidth is 2.6 degrees in the azimuth plane and 3.1 degrees in the elevation plane, which matches the simulated pattern. It is important to note that the pattern multiplication method is less accurate due to no accounting of mutual coupling or edge effects. However, it is significantly more time and resource efficient than full-wave simulations.

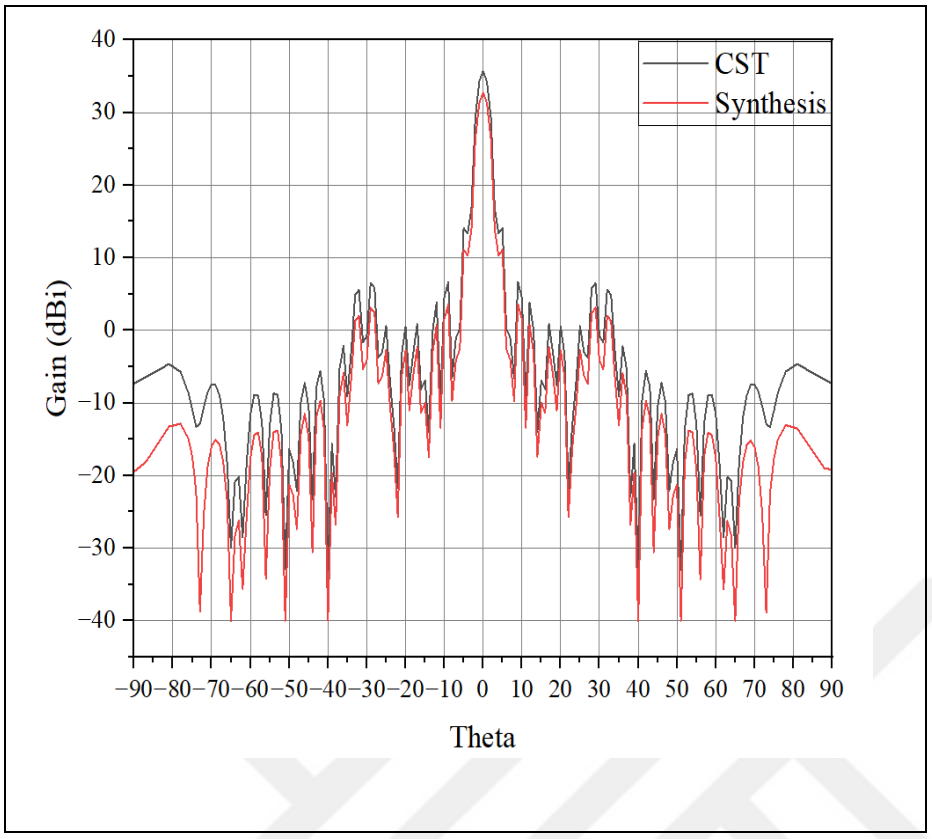
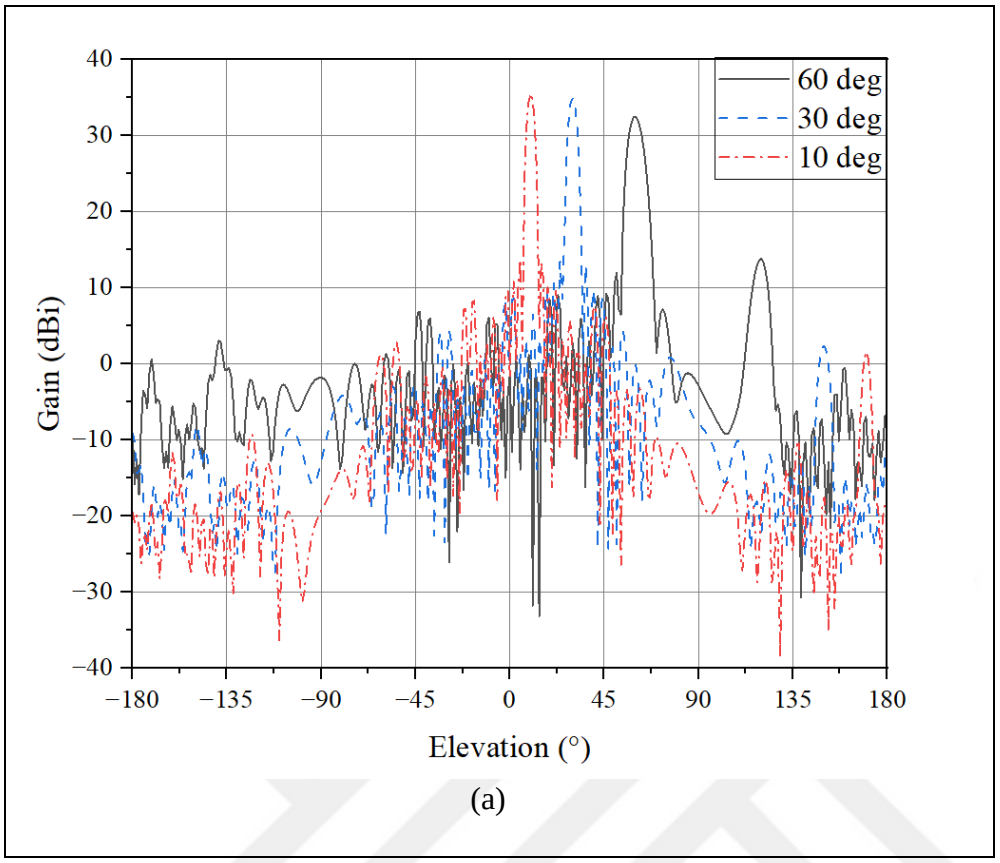


Figure 3.26. CST and synthesized radiation pattern comparison ($\phi = 0$)

The simulated radiation pattern with different scan angles (10°, 30° and 60°) at 10 GHz are shown in Figure 3.27. All results are acquired with uniform illumination of the array. Magnitude of the maximum gain of the antenna at 60-degree scan angle is 32.6 dBi both in azimuth and elevation scan angles, and the side lobe level is about -18.8 dB in elevation scan and -19.3 dB in azimuth scan. 3-dB beamwidth for 60-degree scan angle is 6.5 degrees for elevation scan and 5.6 degrees in azimuth scan. Grating lobe appears behind the antenna at 60-degree scan angle but it is unimportant as it is behind the antenna and does not disrupt the main lobe. The magnitude of the grating lobe is higher in the 60-degree elevation scan angle radiation pattern; therefore, side lobe level is higher than azimuth scan angle as opposed to other scan angles. Array simulation results are summarized at Table 3.6.



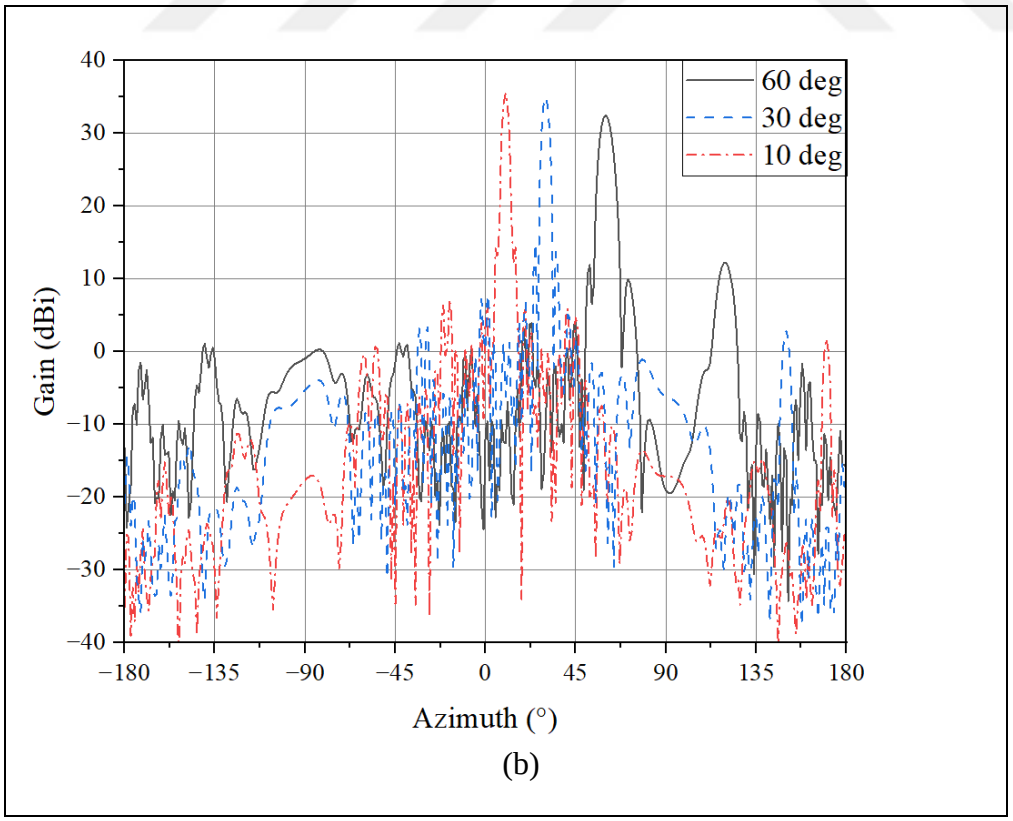


Figure 3.27. Radiation pattern array scanning (a) Elevation scan with different scan angles ($\phi = 90$) (b) Azimuth scan with different scan angles ($\phi = 0$)

Table 3.6. Array radiation patterns summary with different scan angles

Scan Angle Direction (az&el scan)	Main lobe magnitude (dBi) (az&el scan)	SLL (dB) (az/el scan)	3-dB beamwidth (degrees) (az/el scan)
10	35.6	-21.2/-21.8	2.7/3.2
30	35	-20/-21.5	3.1/3.7
60	32.6	-19.3/-18.8	5.6/6.5

3D simulated radiation pattern for 60-degree elevation scan angle is shown in Figure 3.28.

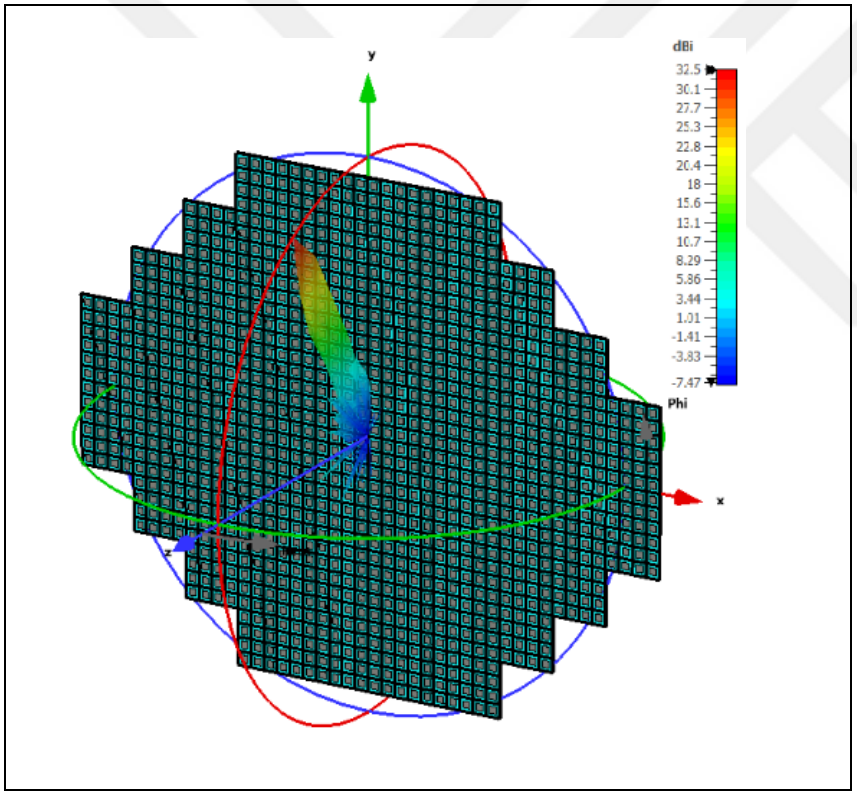


Figure 3.28. 3D radiation pattern for 60-degree elevation scan angle

The array is reconstructed using the unit cell design described in Section 3.2 and is analyzed again. The radiation patterns with and without the feed network are compared and shown in Figure 3.29. The maximum gain and beamwidth of the antenna remain the same, but the array designed with the feed network has poorer SLLs and back lobes due to imperfections in the underside feed network.

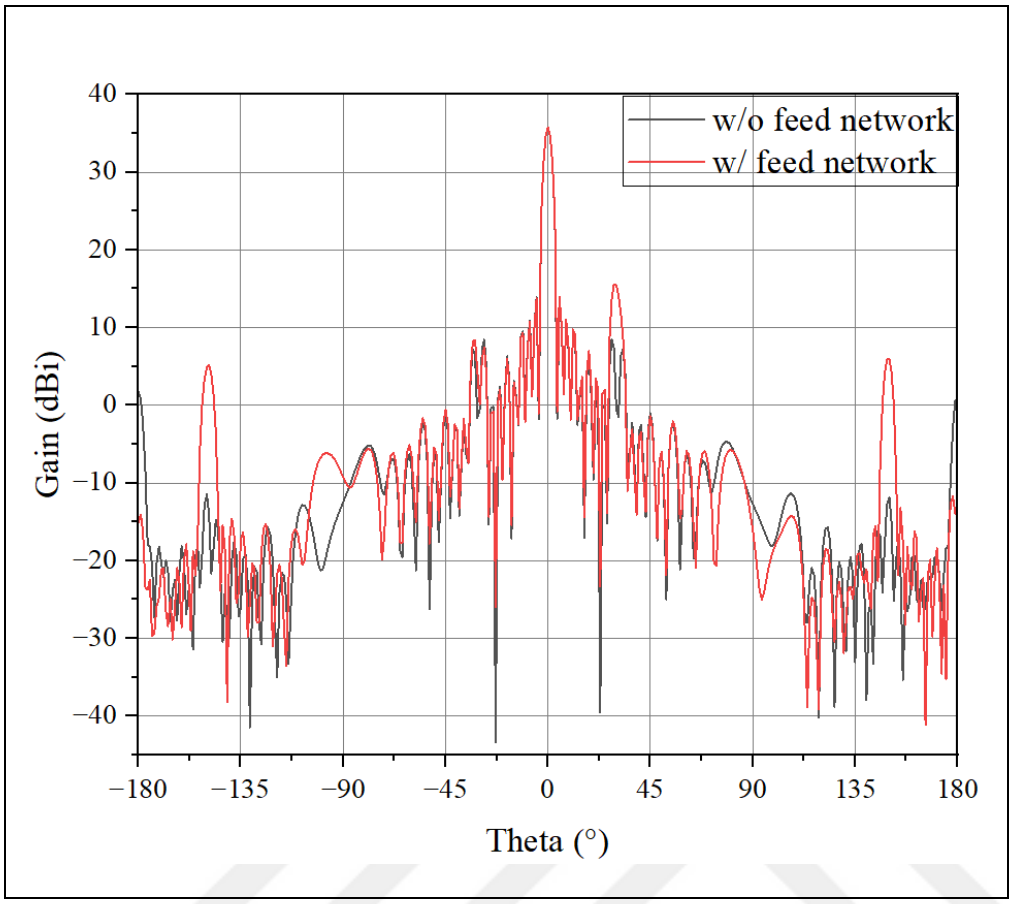


Figure 3.29. Radiation pattern with and without feed network ($\phi = 90$)

3.4. Monolithic Radome Design

Radome is necessary for protecting the array face from environmental effects and to avoid damages when handling the antenna. A radome is ideally electromagnetically transparent in radar's frequency band. The array face radome is obviously not exposed to extreme conditions as the outer aircraft radome, its electrical transparency is of greater importance.

Radome's have critical effects on an antenna's radiation characteristics. Beam deflection, which is the shift of the main lobe from the main axis, is particularly critical for fire control radars. Insertion loss is a measure of signal loss due to reflections and absorption. Reflection of power can cause a shift in the antenna's impedance characteristics, leading to mismatches and sidelobes [18].

Single-layer radomes are simple to design and are extensively used in these applications. Material selection depends on the specific application, but typical materials include

fiberglass, ceramics, elastomers, and foam [18]. Determining the thickness of the radome involves trade-offs. A thin-layer radome is advantageous for wide frequency bandwidth, low insertion loss, and reduced indifference to incident angle and polarization. However, thinner radomes have poorer mechanical strength [41]. The structural limitations of a thin-wall radome can be addressed by using a half-wave wall radome. This design employs a homogeneous dielectric material with an electrical thickness equal to half a wavelength, or a multiple of it, at the relevant incidence angle. However, bandwidth of these types of radome is limited as is the insensitivity to incidence angles [18].

To simulate the effect of a radome on an antenna's radiation characteristics and its impact on the RCS, a single-layer or monolithic radome has been designed and simulated using full-wave simulator.

A monolithic electrically transparent in-band radome using a thermoplastic material (G-10) has been designed. The material has relative permittivity of ε_r= 4.8 and a loss tangent of $tan\delta = 0{,}008$. The length and width of the radome for analysis is the same as the array. The initial wall thickness of the radome has been computed using Eq. (3.7 and further optimized using CST MWS [42].

$$d = \frac{m\lambda}{2}\sqrt{\varepsilon - \sin^2\theta} \tag{3.27}$$

Where λ is the operation wavelength, θ is the incidence angle, ε is the dielectric constant of the material, and m is an integer. The optimized radome has a wall thickness of 7 mm for the best loss performance, and the distance between the array face and the radome is also 7 mm. A single tile radome with dimensions of 59 mm in width and 61 mm in length is simulated, and the insertion loss plot for the boresight incidence angle for TE polarization is shown in Figure 3.30. The insertion loss is lower than -0.1 dB at the antenna's operating frequency, which is very low.

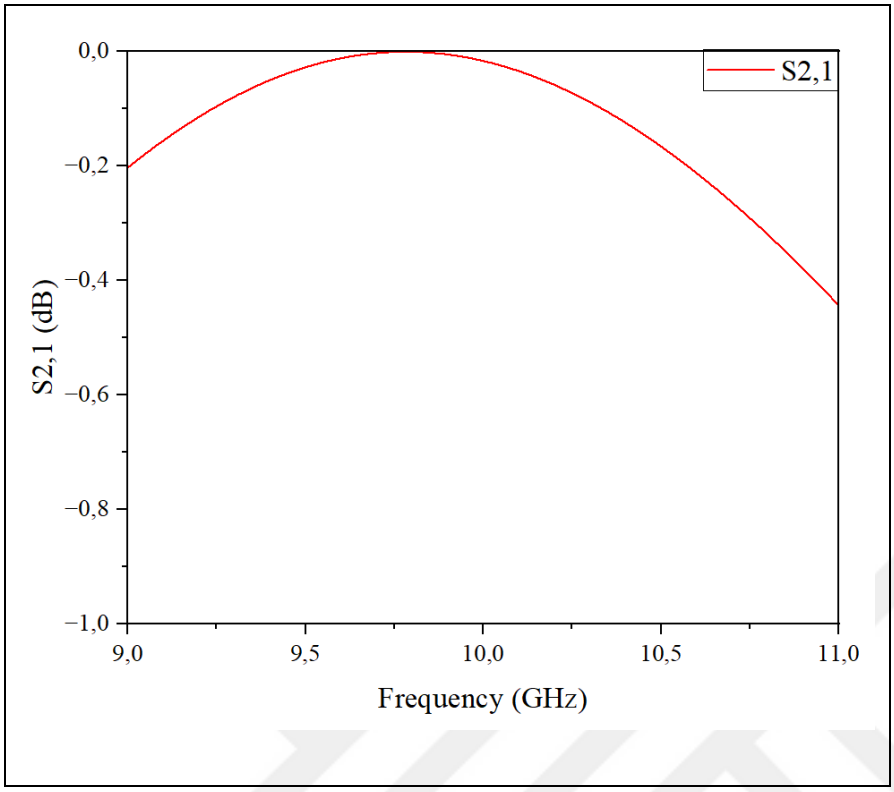


Figure 3.30. Insertion loss S_{21} plot

Figure 3.31. Shows the radiation patterns with and without the radome. It is observed that the maximum gain with the radome is approximately 0.16 dB lower than without it. There is no degradation in the side lobe level, and only a slight degradation in beamwidth is observed.

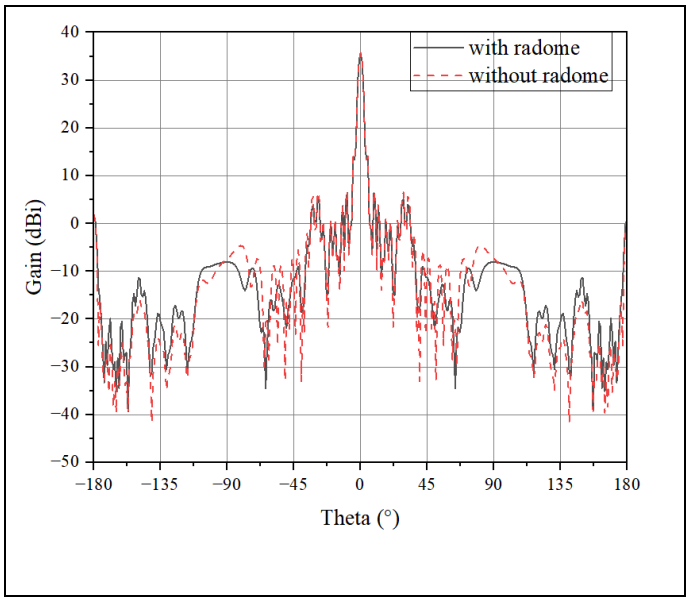


Figure 3.31. Effect on full array radiation performance ($\phi = 0$, f = 10 GHz)

4. ANTENNA RCS THEORY AND RESULTS

4.1. Antenna RCS Computed from Gain

The antenna RCS has an established relationship with antenna's gain due to the antenna's reradiation characteristics. Hansen derives the relationship with antenna gain and antenna mode RCS for a hypothetical antenna that has only antenna mode scattering. Let us assume an antenna with effective aperture A_e is illuminated by a plane wave with a power density of S_i, received power by the antenna would be [7]

$$P_r = S_i Ae \tag{4.1}$$

If the antenna is terminated with a short circuit load ($Z_L = \infty$), there would be exact reflection of the received power, therefore reradiated power would be equal to received power of the antenna. Radiated power density at range R is equal to radiated power divided by area of the sphere ($4\pi R^2$) for isotropic antennas. However, isotropic antennas are unrealizable therefore the reradiated power density is given by [7]

$$S_r = P_r G \,/\, (4\pi R^2) = S_i A_e G \,/\, (4\pi R^2) \tag{4.2}$$

RCS formula can be redefined in terms of power densities rather than electric fields as

$$\sigma = \lim_{R\to\infty} (4\pi R^2)(|E_s|^2/|E_i|^2) = \lim_{R\to\infty} (4\pi R^2)(S_r/S_i) \tag{4.3}$$

Inserting 4.2. into 4.3. gives

$$\sigma = A_e G \tag{4.4}$$

Replacing A_e by

$$A_e = \frac{G\lambda^2}{4\pi} \tag{4.5}$$

Gives the definition of the scattered field due to antenna mode RCS.

$$\sigma = \frac{G^2\lambda^2}{4\pi} \tag{4.6}$$

This definition only represents the antenna mode scattering and ignores structural mode scattering. This definition only assumes that scattered field is due to energy field been collected from free space and traveled down antenna transmission line and re-radiated. Therefore it does not fully represent antenna RCS. The correct computation of antenna RCS must consider both antenna mode and structural mode scattering. This derivation also assumes antenna is terminated with a matched load, however in practice antenna is terminated with a load that absorbs most of the received energy. We can also deduce from the definition that in band RCS may be alot different than out of band RCS, due to gain is being specified at the frequency of the incident wave [3].

4.2. Antenna Scattered Field as a Function of Load Impedance

Scattered field of an antenna is defined in terms of its load impedance as [43]

$$E_s(Z_L) = E_s(Z_L = 0) - \left[\frac{I(0)Z_L}{Z_A + Z_L}\right]E_r \tag{4.7}$$

Where $E_s(Z_L = 0)$ is the scattered field when antenna is terminated with short circuit, $I(0)$ is the short-circuit antenna current induced by the incident field, Z_A is the characteristic impedance of the antenna, and E_r is the radiated field normalized by the antenna driving current.

If the antenna reflection coefficient is defined as:

$$\Gamma_a = \frac{Z_a - Z_L}{Z_a + Z_L} \tag{4.8}$$

Expression (4.7 can be rewritten in terms of reflection coefficient as

$$E_s(Z_L) = E_s(0) - [I(0)(1 - \Gamma_A)/2]E_r \tag{4.9}$$

Scattered field is proportional to square root of RCS, so Eq. (4.9 can be rewritten as

$$\sigma = |\sqrt{\sigma_s} - (1 - \Gamma_A)\sqrt{\sigma_r}\mathrm{e}^{\mathrm{i}\phi}|^2 \tag{4.10}$$

σ_s and σ_r terms are called the structural mode and antenna mode RCS respectively, and ϕ is the relative phase between the terms. The first term is the RCS of the antenna when the antenna is terminated with a short circuit load. The second term subtracts the part that is not re-reradiated by the load. By this definition, a short circuit load ($\Gamma_A = 1$) RCS simply equals to the first term. When antenna is terminated with a matched load ($\Gamma_A = 0$), RCS equals to antenna scattering due to reradiation is removed from the first term [43].

A more intuitive definition is made by [44] for scattered field in terms of conjugate matched load and matched load current as

$$E_s(Z_L) = E_s(Z_a^*) + [I(0)\Gamma_A^*/2]E_r \tag{4.11}$$

Where conjugate matched load current is $I_m^* = I(0)/2$, therefore

$$E_s(Z_L) = E_s(Z_A^*) + I_m^*\Gamma_A^* E_r \tag{4.12}$$

Where,

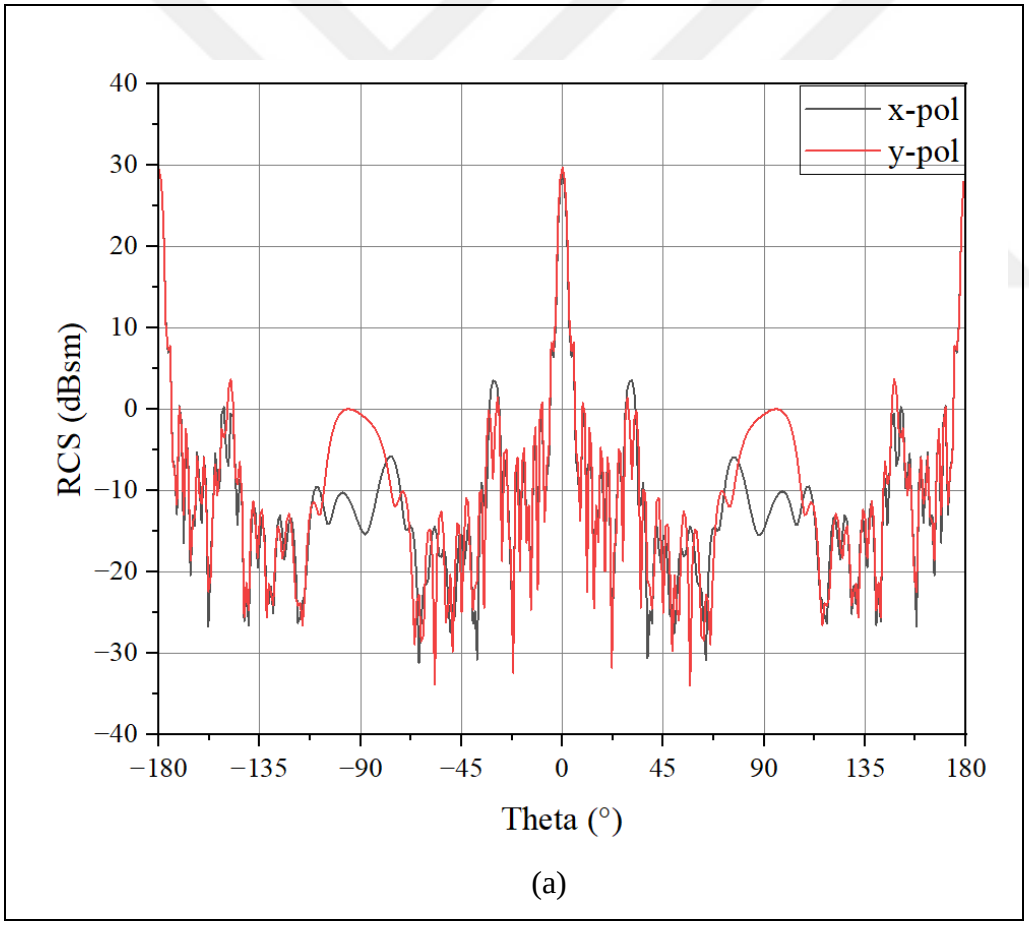
$$\Gamma_a^* = (Z_A^* - Z_L)/(Z_A + Z_L) \tag{4.13}$$

Green defines the first term as the structural mode RCS and the second term as the antenna mode RCS. From this definition, the structural term is deduced to be independent of the antenna load impedance. When the antenna is terminated with a matched load, scattering arises solely due to the antenna's physical properties. The second term is related to the antenna's radiation pattern and completely vanishes if the antenna is conjugately matched.

4.3. Antenna RCS Results

The structural mode RCS has been analyzed when array ports are terminated with a matched load using time domain simulations in CST. Matched load RCS patterns are shown in Figure 4.1. at 10 GHz in both planes. All the simulations in these plots carried

out without radome included and using the full array designed with the unit cell designed in Section 3.2. Each plot includes RCS patterns for two plane waves with different polarizations, i.e., the incident plane wave polarized in x-axis and y-axis. The plane wave is incident on boresight direction to simulate the worst-case scenario in terms of RCS. When a y-polarized plane wave is incident, the scattering field is more dominant in the elevation plane. Consequently, the antenna exhibits the worst scattering performance under y-polarized waves. When the antenna is terminated with a matched load, it shows indifference to the antenna's radiation characteristics. Therefore, changing the characteristic impedance of the antenna has no effect on the structural mode RCS. The peak RCS for a y-polarized wave is 29.75 dBsm, while for an x-polarized wave, it is 29.01 dBsm.



(a)

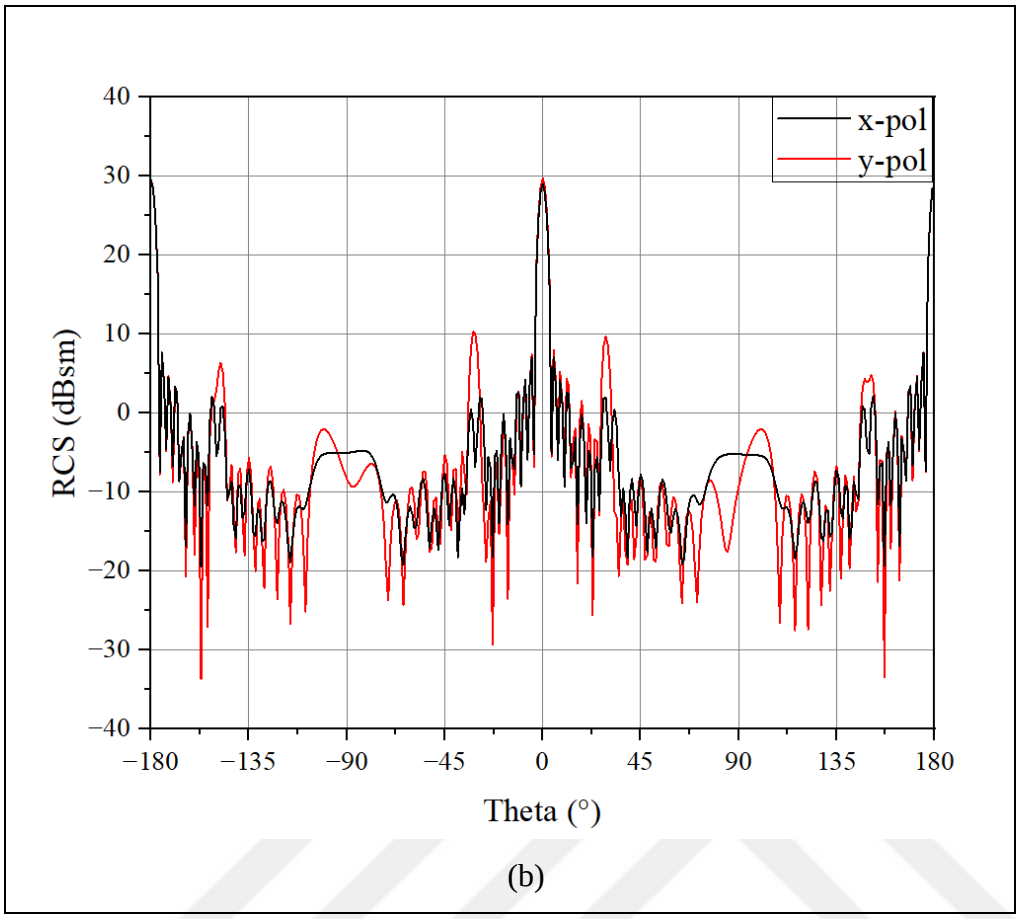


Figure 4.1. Matched load RCS pattern with different polarized incident waves at f=10 GHz (a) ($\phi = 0$) (b) ($\phi = 90$)

The radome included scattering pattern in both planes and plane waves with different polarizations is shown in Figure 4.2. The peak RCS for a y-polarized wave is 29.29 dBsm, while for an x-polarized wave, it is 29.74 dBsm. As it is expected radome has minimal effect on the RCS of the array due to its electrically transparent characteristics.

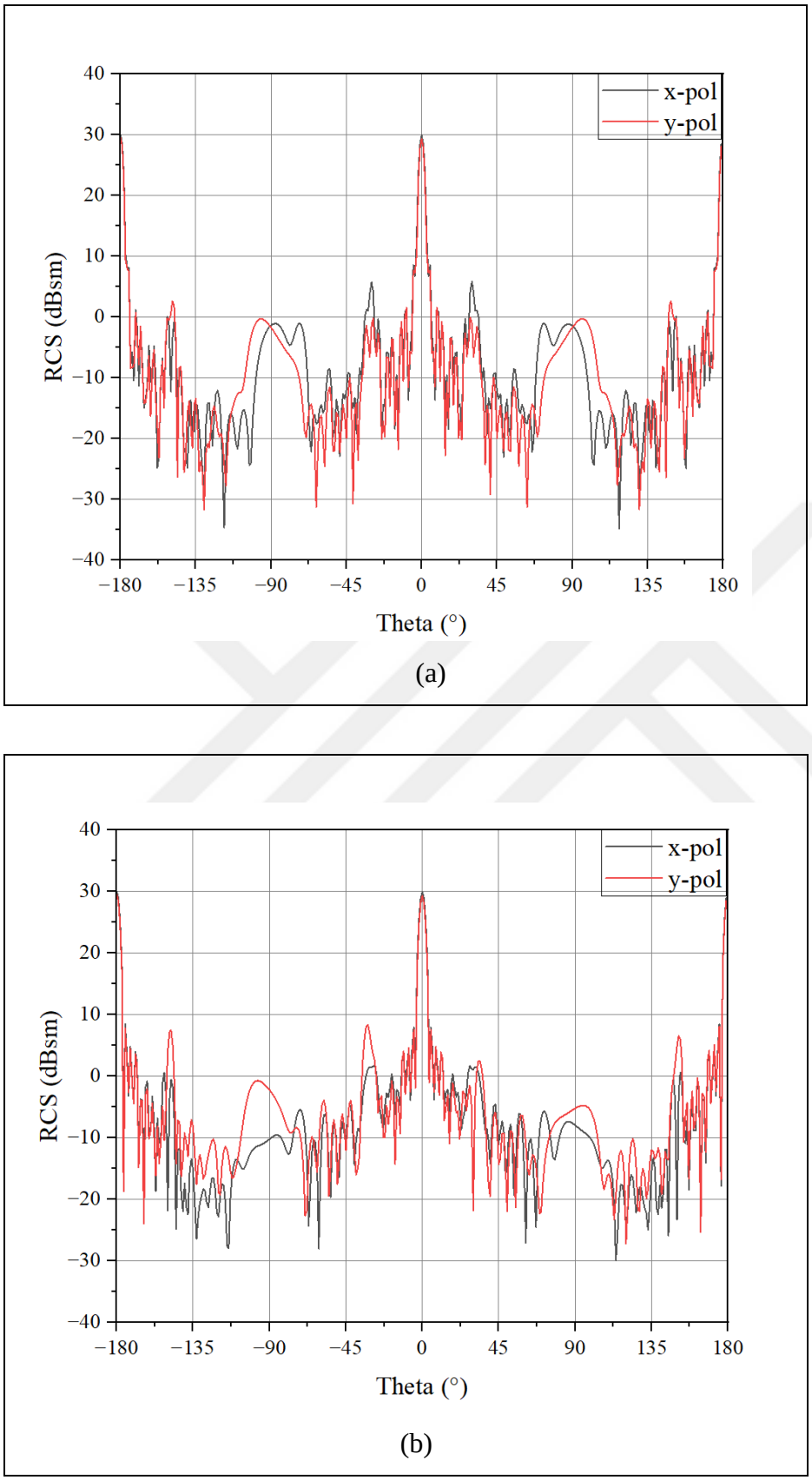


Figure 4.2. Matched load RCS pattern with radome and different polarized planes waves at f=10 GHz (a) ($\phi = 0$) (b) ($\phi = 90$)

3D RCS pattern of the array antenna with radome is shown in Figure 4.3.

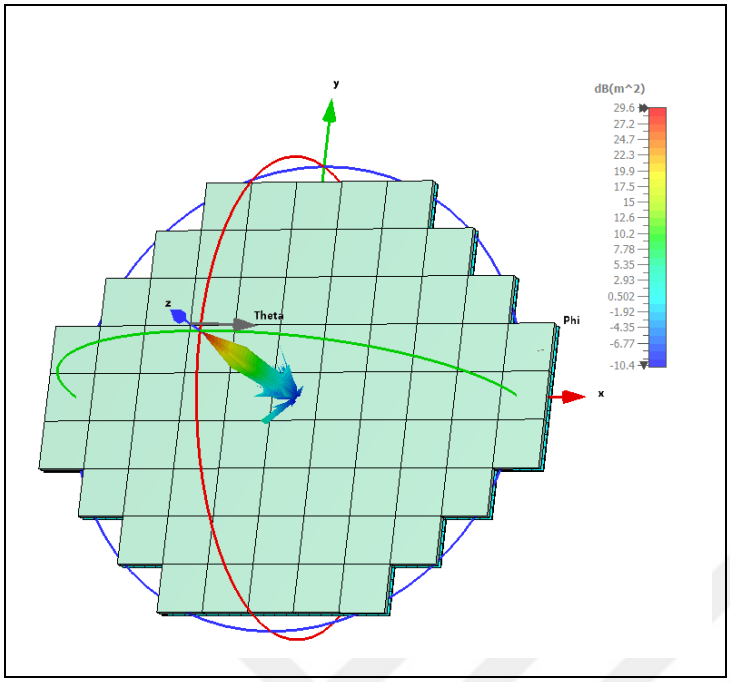


Figure 4.3. Scattering 3D pattern under y-polarized incident wave (antenna w/ radome)

Structural mode RCS versus frequency for y-polarized plane wave incident on broadside direction in monostatic configuration is shown in Figure 4.4. The backscattering, when the antenna is match-loaded, generally increases with frequency. Additionally, the radome has minimal effect on the structural RCS of the antenna.

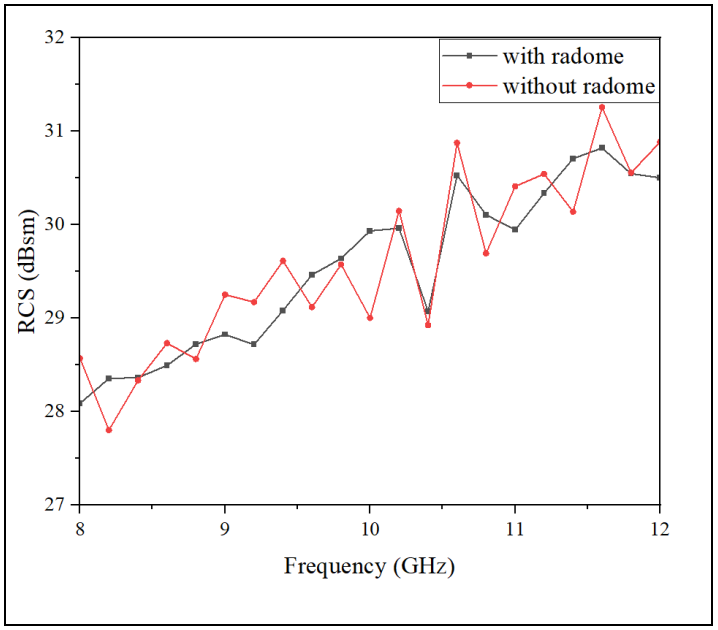


Figure 4.4. Matched load RCS versus frequency with and without radome.

It is reported that tilting the array upwards can significantly reduce antenna RCS in the incident wave direction. Most modern fighter platform AESA radars are installed to the platform this way to avoid mirror like reflections to the enemy radar [15]. The tilt does not reduce the antenna scattering but redirects it to a non-harmful direction. Effect of tilting the antenna on the reflections shown in Figure 4.5.

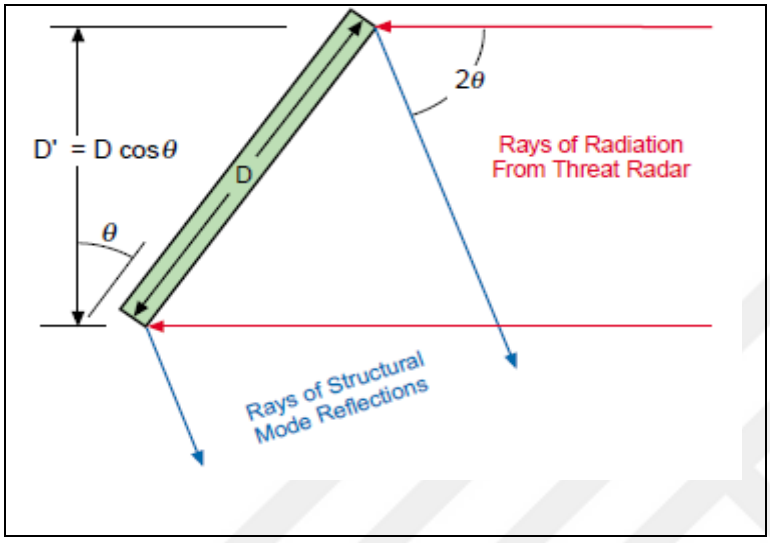


Figure 4.5. Effect of tilting the array on structural mode scattering [15]

To simulate the effect of tilting on structural mode RCS, plane wave incident on $\phi = 90°$, $\theta = -20°$ direction is simulated and shown in Figure 4.6. It is observed that structural RCS is reduced more than 30 dB in the broadside direction and main lobe is on -42 degrees with a magnitude of 25.38 dBsm.

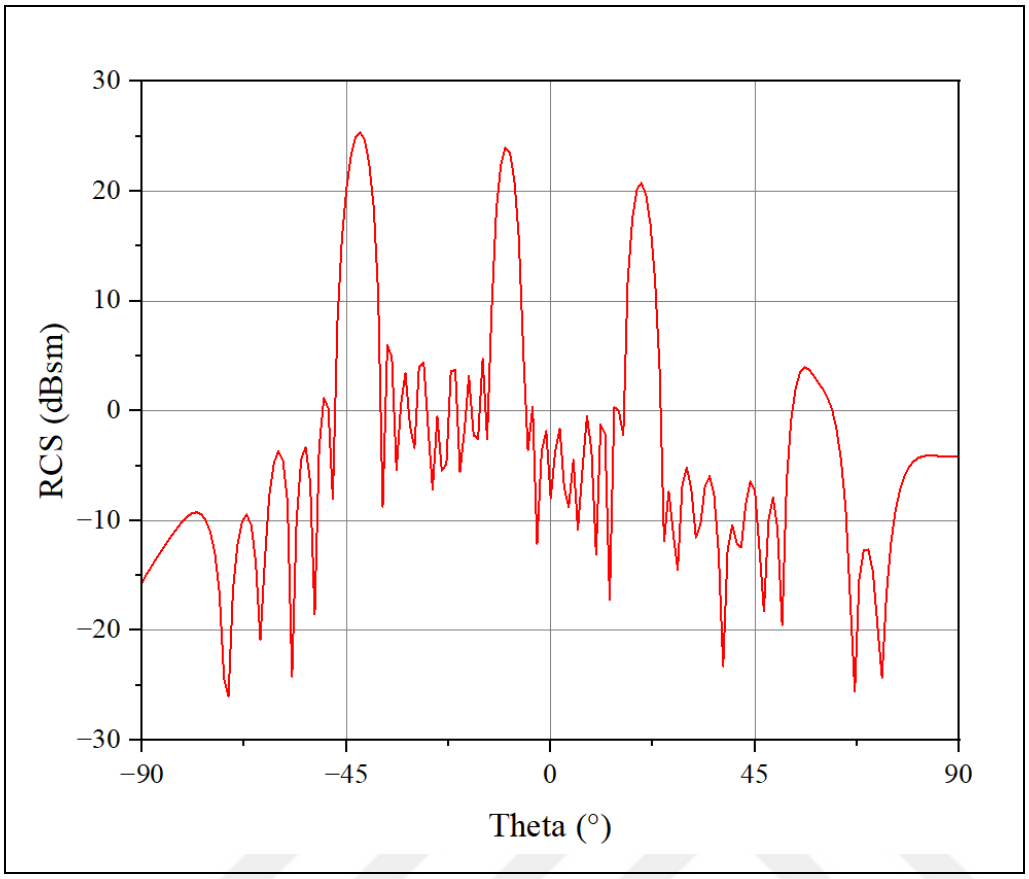
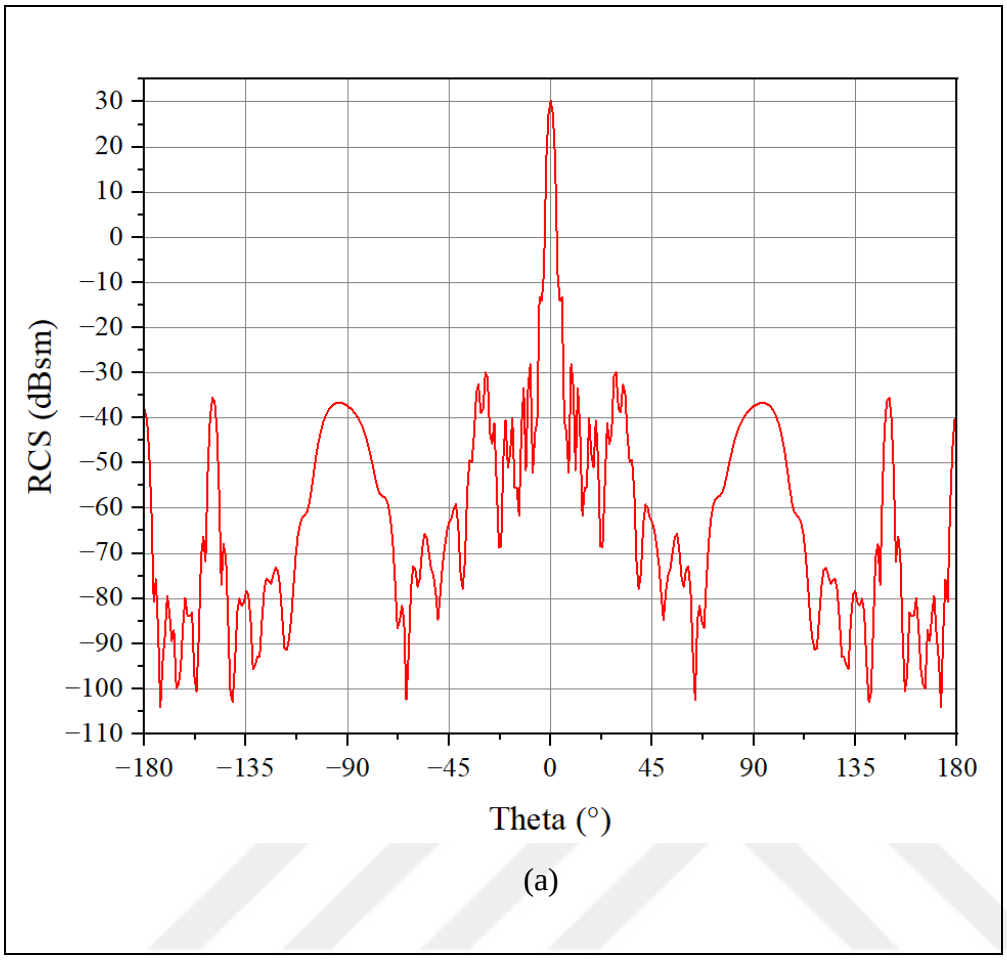


Figure 4.6. ML-RCS when plane wave incident on ϕ=90°, θ=-20° at 10GHz (xz plane)

Antenna mode RCS has been computed using the gain reconstruction method mentioned earlier in the chapter using the gain data obtained with full wave simulations and shown in Figure 4.7. on both planes. The data shown is for configuration is with the radome and underside corporate feed network is implemented. The antenna mode RCS results with under conditions are shown in Figure 4.8. These conditions include the antenna is with and without the radome, and with and without the underside corporate feed network. It is observed that antenna mode RCS in broadside direction is nearly identical but slightly higher at 30,27 dBsm in worst case condition but much lower at other directions. The sidelobes magnitudes are generally higher on configurations with feed network than those without due to imperfections on the feed network.



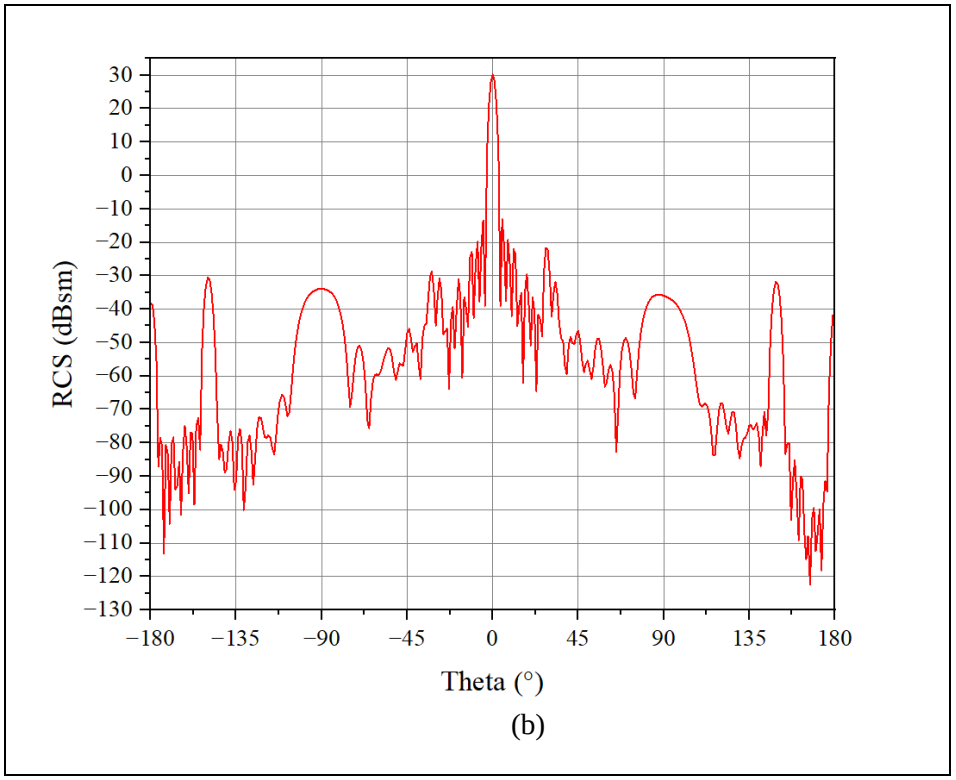


Figure 4.7. Antenna mode RCS radome and feed network included (a) ϕ = 0° (b) ϕ =90°

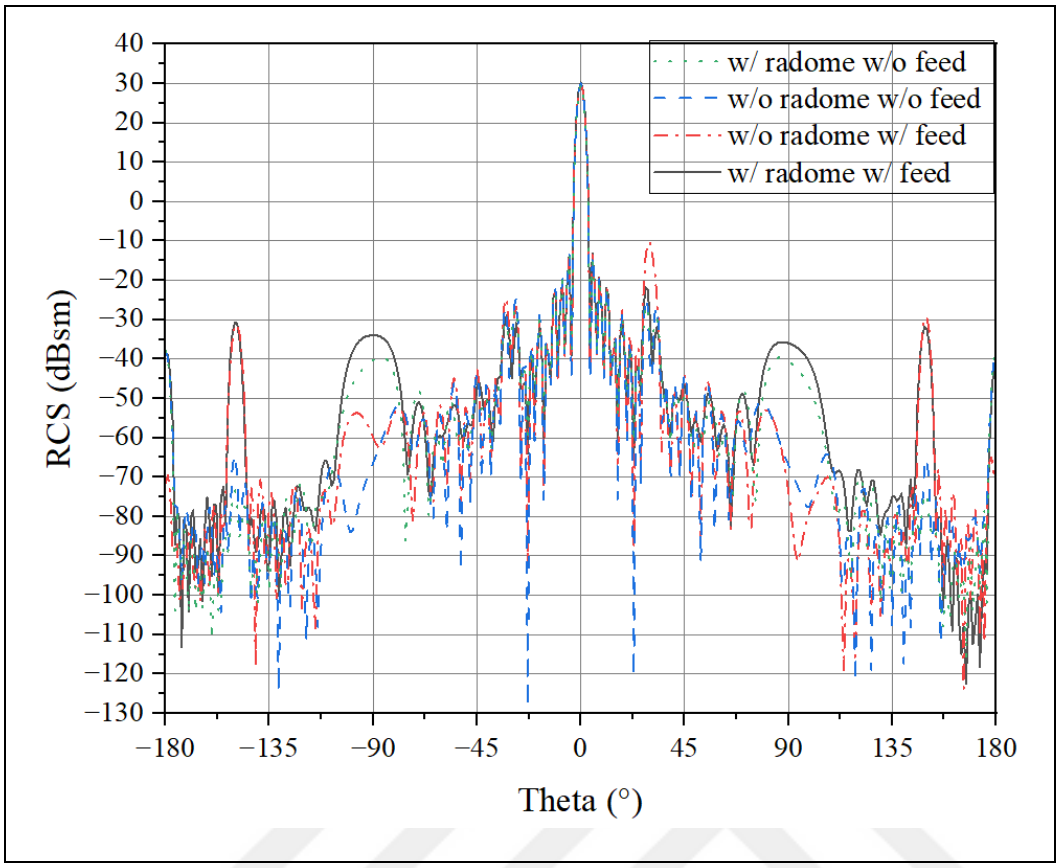


Figure 4.8. Antenna mode RCS with different configurations (ϕ = 90°)

The direction of the main lobe of the antenna mode RCS is influenced by the angle of incidence and the phase shift between elements in the array. Therefore, tilting the array does not mitigate the antenna mode RCS. Instead, the antenna mode RCS can be effectively reduced by implementing well-matched circuitry within the system, which minimizes reflections and mismatch losses. Additionally, designing a low sidelobe array can help in reducing the RCS by minimizing the radiation and scattering in unwanted directions, thereby decreasing the overall visibility of the antenna to radar detection. These strategies collectively help in optimizing the antenna's performance and reducing its RCS [15].

5. CONCLUSION

In this thesis study, an AESA-type phased array antenna model has been designed, and its radiation and scattering characteristics have been analyzed using a full-wave simulator tool. A scalable array antenna consisting of 1,200 stacked patch antenna elements was designed. When uniformly illuminated, the antenna features a peak gain of 35.75 dBi, a -10 dB active element impedance bandwidth of 12%, SLL lower than -20 dB, a 3 dB beamwidth of 2.6 degrees in the azimuth plane and 3.1 degrees in the elevation plane, grating lobe-free forward semi-circle beam steering, and good polarization isolation. The dimensions and geometry of the array were chosen to be compatible with the F-16 platform for realistic analysis.

An underside corporate feed network was designed for a single tile module, along with a radome to simulate the effect on the radiation pattern and antenna RCS. Both structural mode and antenna mode scattering were analyzed. It was concluded that an electrically-transparent radome can have a minimal effect on RCS. Additionally, it was found that transmission losses in the feed network can substantially affect the array's radiation and scattering. Structural mode RCS was found to be dominant over antenna mode RCS in the side lobes, while the main lobe exhibited similar characteristics. Both modes were observed to have a peak RCS of up to 30 dBsm. Additionally, the RCS in the observer direction can be reduced by more than 30 dB by tilting the antenna upwards, thereby shifting the main lobe to a no-threat area.

This study is useful for demonstrating the significance of scattering in AESAs and for understanding and analyzing the RCS of array antennas. Furthermore, suggestions are made throughout the study to mitigate the RCS of array antennas.

REFERENCES

1. Skolnik, M. I. (2008). *Radar Handbook*, (Third Edition). New York: McGraw-Hill Education.

2. Farina, A., Holbourn, P., Kinghorn, T., and Timmoneri, L. (2013). *AESA Radar — Pan-domain multi-function capabilities for future systems*. In 2013 IEEE International Symposium on Phased Array Systems and Technology.

3. Knott, E. F., Shaeffer, J., and Tuley, M. T. (2004). *Radar cross section*. Institution of Engineering and Technology eBooks.

4. Gou, Y., Chen, Y., and Yang, S. (2022). Radar cross section reduction of wideband Vivaldi antenna arrays with Array-Level scattering cancellation. *IEEE Transactions on Antennas and Propagation*, 70(8), 6740–6750.

5. Tian, N. W., Hou, N. X., and Che, N. Y. (2013). *The analysis and measurement of FSS radome for antenna RCS reduction*. In 2013 Cross Strait Quad-Regional Radio Science and Wireless Technology Conference, Chengdu.

6. Shin, H., Yoon, D., Na, D., and Park, Y. B. (2022). Analysis of Radome cross section of an aircraft equipped with a FSS Radome. *IEEE Access*, 10, 33704–33712.

7. Appel-Hansen, J. (1979). Accurate determination of gain and radiation patterns by radar cross-section measurements, *IEEE Trans. on Ant. and Prop.*, AP-27, (5), pp.640-646.

8. Pozar, D. (1987). Radiation and scattering from a microstrip patch on a uniaxial substrate. *IRE Transactions on Antennas and Propagation/I.R.E. Transactions on Antennas and Propagation*, 35(6), 613–621.

9. Jiang, W., Liu, Y., Gong, S., and Hong, T. (2009). Application of Bionics in antenna radar cross section reduction. *IEEE Antennas and Wireless Propagation Letters/Antennas and Wireless Propagation Letters*, 8, 1275–1278.

10. Hu, S., Chen, H., Law, C. L., Shen, Z., Li, Z., Zhang, W., and Wang, D. (2007). Backscattering cross section of ultrawideband antennas. *IEEE Antennas and Wireless Propagation Letters/Antennas and Wireless Propagation Letters*, 6, 70–73.

11. Liu, Y., Fu, D., and Gong, S. (2003). A novel model for analyzing the radar cross section of microstrip antenna. *Journal of Electromagnetic Waves and Applications*, 17(9), 1301–1310.

12. Liu, Y., and You, L. (2011b). *Research on the estimation and reduction measures of antenna mode RCS of airborne phased array*. In 2011 4th IEEE International Symposium on Microwave, Antenna, Propagation and EMC Technologies for Wireless Communications.

13. J Gan, L., Jiang, W., Chen, Q., Li, X., Zhou, Z., and Gong, S. (2021). Method to estimate antenna mode radar cross section of Large-Scale array antennas. *IEEE Transactions on Antennas and Propagation*, 69(10), 7029–7034.

14. Wang, Y., and Cao, L. (2013b). *Status in U.S. AESA Fighter Radar and Development Trends*. In IET International Radar Conference 2013, Xi'an.

15. Stimson, G. W. (1998). *Introduction to airborne radar.* Mendham: Institution of Engineering and Technology eBooks.

16. Balanis, C. A. (2005). *Antenna theory: Analysis and design.* Hoboken: John Wiley and Sons.

17. Lyon, R. (2008). *Radiating elements for wideband electronically scanned arrays*. Institution of Engineering and Technology Seminar on Wideband, Multiband Antennas and Arrays for Defence or Civil Applications, London.

18. Skolnik, M. I. (1980). *Introduction to Radar Systems*. Auckland: McGraw-Hill Companies.

19. Mark A. Richards, M. I. (2010). *Principles of Modern Radar: Basic principles*. London: Institution of Engineering and Technology eBooks.

20. Brookner, E. (2008). *Phased-array and radar astounding breakthroughs - An update.* In 2008 IEEE Radar Conference, Rome.

21. Ruck, G. T. (1970). *Radar cross section handbook, vol. 2,* New York: Plenum Press.

22. Güngördü, Ö. B., Kara, A., and Akşimşek, S. (2024). A complementary overview and challenges in radar cross section modeling of phased array antennas. *Journal of Science, Technology and Engineering Research,* 5(1), 86-91.

23. Vasanelli, C., Bogelsack, F., and Waldschmidt, C. (2018). Reducing the radar cross section of microstrip arrays using AMC structures for the vehicle integration of automotive radars. *IEEE Transactions on Antennas and Propagation,* 66(3), 1456–1464.

24. Noorbakhsh, B., Abdolali, A., and Janforooz, M. (2021). In-band radar cross-section reduction of the slot array antennas by RAM-based frequency selective surfaces. *IET Microwaves, Antennas & Propagation,* 15(5), 457–463.

25. Wang, X., Tong, X., Wang, J., A, S., Wang, J., and Han, X. (2024). A polarization-converting metasurface for reducing radar cross sections and enhancing radiation performance of circularly polarized array antennas. *Optics Communications*, 556, 130269.

26. Lu, Y., Su, J., Liu, J., Guo, Q., Yin, H., Li, Z., and Song, J. (2019). Ultrawideband monostatic and bistatic RCS reductions for both copolarization and cross polarization based on polarization conversion and destructive interference. *IEEE Transactions on Antennas and Propagation*, 67(7), 4936–4941.

27. Li, K., Liu, Y., Jia, Y., and Guo, Y. J. (2017). A circularly polarized High-Gain antenna with low RCS over a wideband using chessboard polarization conversion metasurfaces. *IEEE Transactions on Antennas and Propagation*, 65(8), 4288–4292.

28. Ji, L., Hong, X., Yang, R., Liu, Q., and Zhang, W. (2024). A low radar cross section antenna array based on a liquid metal metasurface. *IET Microwaves, Antennas & Propagation*, 18(3), 173–180.

29. Zhao, C., Jiang, W., Ge, J., Xi, Y., Hong, T., and Gong, S. (2021). A low-radar cross section Vivaldi antenna array based on reflection cancelation. *International Journal of RF and Microwave Computer-aided Engineering*, 32(3), 6740-6750.

30. Fang, S., Qu, S., Yang, S., and Hu, J. (2023). Low-Scattering X-Band Planar Phased Vivaldi Array antenna. *IEEE Transactions on Antennas and Propagation*, 71(3), 2808–2813.

31. Mailloux, R. J. (1993). *Phased Array Antenna Handbook*. Norwood: Artech House

32. Waterhouse, R. (1999). Design of probe-fed stacked patches. *IEEE Transactions on Antennas and Propagation*, 47(12), 1780–1784.

33. Anguera, J., Puente, C., and Borja, C. (2003). *A procedure to design wide-band electromagnetically-coupled stacked microstrip antennas based on a simple network model*. In IEEE Antennas and Propagation Society International Symposium. 1999 Digest. Held in conjunction with: USNC/URSI National Radio Science Meeting

34. Bahl, I. J. and Bhartia, P. (1980). *Microstrip Antennas* (1st ed.). Norwood: Artech House.

35. Matin, M., Sharif, B., and Tsimenidis, C. (2007). Dual layer stacked rectangular microstrip patch antenna for ultra-wideband applications. *IET Microwaves, Antennas & Propagation*, 1(6), 1192.

36. Potok, M. (1980). Microwave devices and circuits. *Electronics Power*, 26(7), 592.

37. Mailloux, R. (1992). Antenna array architecture. *Proceedings of the IEEE*, 80(1), 163–172.

38. Porras, M. J. P., Bertuch, T., Loecker, C., Adams, R. J., Wunderlich, R., and Heinen, S. (2015). An AESA antenna comprising an RF feeding network with strongly coupled antenna ports. *IEEE Transactions on Antennas and Propagation*, 63(1), 182–194.

39. Pozar, D. (1994). The active element pattern. *IEEE Transactions on Antennas and Propagation*, 42(8), 1176–1178.

40. Rutschlin, M., Wittig, T., and Iluz, Z. (2016). *Phased antenna array design with CST STUDIO SUITE*. In 2016 10th European Conference on Antennas and Propagation (EuCAP), Davos.

41. Shavit, R. (2018). *Radome Electromagnetic Theory and Design*. Hoboken: John Wiley & Sons Ltd.

42. Lakshmaiah, A., Prasad, N., and Ray, K. (2021). Investigations on Monolithic Radome Interactions with Active Electronically Scanned Array on Fighter Platform. *Defence Science Journal/Defence Science Journal*, 71(5), 662–669.

43. Hansen, R. (1989). Relationships between antennas as scatterers and as radiators. *Proceedings of the IEEE*, 77(5), 659–662.

44. Green, R. (1966). Scattering from conjugate-matched antennas. *IRE Transactions on Antennas and Propagation/I.R.E. Transactions on Antennas and Propagation*, 14(1), 17–21.



Gazili olmak ayrıcalıktır